Aerial Vehicle Protection Level Reduction by Fusing GNSS and Terrestrial Signals of Opportunity

Mahdi Maaref, Joe Khalife, *Member, IEEE*, and Zaher M. Kassas, *Senior Member, IEEE*

***Abstract*— A method for reducing the protection levels (PLs) of aerial vehicles by fusing global navigation satellite systems (GNSS) signals with terrestrial signals of opportunity (SOPs) is developed. PL is a navigation integrity parameter that guarantees the probability of position error exceeding a certain value to be bounded by a target integrity risk. For unmanned aerial vehicles (UAVs), it is desirable to achieve as tight PLs as possible. This paper characterizes terrestrial cellular SOPs' measurement errors from extensive UAV flight campaigns, collected over the past few years in different environments and from different providers, transmitting at different frequencies and bandwidths. Next, the reduction in PLs due to fusing terrestrial SOPs with a traditional GNSS-based navigation system is analyzed. It is demonstrated that incorporating terrestrial SOP measurements is more effective in reducing the PLs over adding GNSS measurements. Experimental results are presented for a UAV traversing a trajectory of 823 m, during which the VPL of the GPS-based and GNSS-based navigation systems were reduced by 56.9% and 58.8%, respectively, upon incorporating SOPs; while the HPL of the GPS-based and GNSS-based navigation systems were reduced by 82.4% and 74.6%, respectively, upon incorporating SOPs.**

***Index Terms*— Integrity, protection level, signals of opportunity, GNSS, navigation, UAV.**

I. INTRODUCTION

AVIATION is undergoing a monumental transformation with the introduction of unmanned aerial vehicles (UAVs) into the national airspace. UAVs promise to create a significant number of technical jobs and transform numerous industries, such as construction, surveying, transportation, delivery, agriculture, entertainment, among others [1]. Moreover, UAVs can be tasked with hazardous and humanly prohibitive tasks, such as infrastructure inspection, hurricane relief, and firefighting. As UAVs perform increasingly complex tasks in a semi-autonomous or a fully-autonomous fashion, the requirements on the accuracy and safety of their navigation system become ever more stringent [2].

UAVs are equipped with a suite of sensors with different modalities, including passive signal-based (e.g., global navigation satellite system (GNSS)) and dead-reckoning (DR) (e.g., inertial navigation system (INS)). These sensing modalities can be classified into two major categories: (i) local sensing modalities, which provide the location of the UAV relative to its own coordinate system and (ii) global sensing modalities, which provide the absolute location of the UAV within a global frame. Navigation systems onboard today's UAVs mainly rely on GNSS, which has monopolized global sensing technologies in outdoor applications for the past few decades. However, GNSS signals are challenged in urban environments [3]–[5] and could be easily compromised via interference, jamming, or spoofing [6], [7]. Integrity monitoring is one criterion to evaluate GNSS performance, which refers to the ability of the navigation system to provide timely warnings when the information given by its on-board sensors is not trustworthy [8]–[11]. Integrity monitoring frameworks are divided into two categories: internal and external [12]. External methods (e.g., ground-based augmentation system (GBAS), satellite-based augmentation system (SBAS), etc.) leverage a network of ground monitoring stations to monitor the transmitted signals, while internal methods (e.g., receiver autonomous integrity monitoring (RAIM)) typically use the redundant information within the transmitted navigation signals.

RAIM checks the consistency in the redundant measurements to perform fault detection and exclusion. RAIM also assesses the availability performance by calculating the vertical and horizontal protection levels (VPL and HPL). By definition, the protection level (PL) is defined as a confidence bound on the size of the position domain error given a specified target integrity risk [13]. Constructing tight PLs (i.e., VPL and HPL) has been the subject of several studies, and many different RAIM schemes incorporating other sensing modalities have been proposed, such as multi-constellation RAIM (e.g., Galileo-GPS [14] and GLONASS-GPS [15]), INS-GPS RAIM [16], and lidar-GPS RAIM [17]. This paper considers exploiting terrestrial signals of opportunity (SOPs) as an additional "constellation" and develops RAIM for SOP-GNSS to reduce the PLs even further. SOPs are ambient radio signals that are not intended for navigation or timing purposes, such as AM/FM radio [18], [19], cellular [20]–[24], digital

Manuscript received March 16, 2020; revised October 4, 2020 and June 8, 2021; accepted June 15, 2021. Date of publication July 16, 2021; date of current version September 1, 2021. This work was supported in part by the Office of Naval Research (ONR) under Grant N00014-19-1-2613, in part by the U.S. Department of Transportation (USDOT) for the CARMEN University Transportation Center (UTC) under Grant 69A3552047138, and in part by the National Science Foundation (NSF) under Grant 1929965. The Associate Editor for this article was E. Atkins. *(Corresponding author: Zaher M. Kassas.)*

The authors are with the Department of Mechanical and Aerospace Engineering, University of California, Irvine, CA 92521 USA (e-mail: mmaaref@uci.edu; khalifej@uci.edu; zkassas@ieee.org).

This article has supplementary downloadable material available at https://doi.org/10.1109/TITS.2021.3095184, provided by the authors.

Digital Object Identifier 10.1109/TITS.2021.3095184

television [25], [26], low Earth orbit (LEO) satellite signals [27]–[30], and Wi-Fi [31], [32]. In contrast to DR-type sensors, *absolute* position information may be extracted from SOPs. Moreover, SOPs are practically unaffected by dense smoke, fog, rain, snow, and other poor weather conditions. SOPs enjoy several inherently desirable attributes: (i) abundance in most locales of interest, (ii) transmission at a wide range of frequencies and directions, (iii) reception at carrier-to-noise ratio that is commonly tens of dBs higher than that of GNSS signals, and (iv) they are free to use, since their infrastructure is already operational [33], [34]. The literature demonstrated the benefit of fusing SOP and GNSS signals to reduce the vertical dilution of precision (VDOP) [35].

This paper proposes a GNSS-SOP RAIM approach, which exploits the favorable transmitter-to-receiver geometry to significantly reduce a UAV's PL. Since all GNSS satellites are typically above the UAV-mounted receiver, GNSS measurements lack elevation angle diversity, which in turn degrades the VPL. In contrast, terrestrial SOP transmitters are inherently at low elevation angles. As a consequence, a combined GNSS-SOP system will benefit from a *doubled* elevation angle range. In addition, certain SOPs possess favorable geometric configurations by construction, e.g., cellular towers are placed at the center of hexagonal cells. This yields well-spaced azimuth angles, which is desirable for HPL reduction.

An initial work that considered fusing GPS and SOP signals for UAV integrity monitoring was conducted in [36]. This paper extends the previous work through the following contributions. First, cellular SOP measurement errors are characterized from hours of UAV flight campaigns over the past few years, which collected extensive SOP data in different environments. The presented SOP measurements represent the most extensive characterization to-date of cellular SOPs in various environments and from different cellular providers, transmitting at different frequencies and bandwidths. Probability density function (pdf) and cumulative distribution function (cdf)-based overbounding are established and compared. Moreover, the SOP measurements' fault rate is calculated. Second, in contrast to the previous work where only GPS signals were considered, the combined GNSS-SOP performance is evaluated in this paper. Third, different sources for SOP measurement error are evaluated, including multipath, clock bias error, and poor geometric conditions. Fourth, a real-world experiment with cellular long-term evolution (LTE) SOPs are presented demonstrating the proposed GNSS-SOP system to reduce the UAV's PLs. The experimental results using eleven cellular LTE SOPs show that the proposed framework reduces the VPL over GPS-based and GNSS-based navigation systems by 56.9% and 58.8%, respectively; while the framework resulted in HPL reduction over GPS-based and GNSS-based navigation systems by 82.4% and 74.6%, respectively.

The structure of this paper is organized as follows. Section II details the motivation and background of this work. Section III formulates the GPS-SOP navigation solution. Section IV studies empirically the salient attributes of the SOP measurements. This methodology can be applied to other terrestrial SOP classes. Section V discusses the enhancement in the RAIM PL by incorporating the SOP measurement. Sections VI and VII present simulation and experimental results with cellular LTE signals, evaluating the efficacy and accuracy of the proposed framework. Concluding remarks are given in Section VIII.

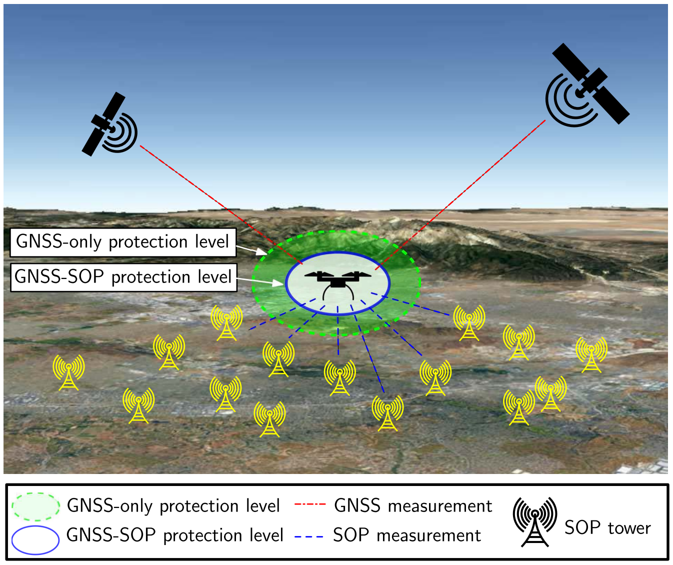

Fig. 1. The proposed method which combines pseudoranges obtained from GNSS satellites and terrestrial SOP transmitters to reduce the PL. Note the abundance of cellular LTE SOPs in this environment: Riverside, California, USA. Many other types of SOPs are also present in the environment but are not plotted here.

II. BACKGROUND AND MOTIVATION

This paper proposes a GNSS-SOP framework for UAV navigation, which significantly reduces the UAV's PL compared to traditional GNSS-based frameworks. The UAV employs a RAIM-based algorithm to calculate the PL. This paper aims at investigating the enhancement in the transmitter-to-receiver geometry, considering the fact that terrestrial SOP measurements are received from negative elevation angles, as the UAV can fly above the terrestrial SOPs. Fig. 1 demonstrates the proposed GNSS-SOP framework. In contrast to GBAS-based frameworks, the expected reduction in PL can be obtained without installing dedicated, costly ground-based stations.

The integrity of GNSS measurements can be established via the navigation message, which specifies anomalies related to satellite operation, such as transmitters' clock errors and satellite service failure. However, the integrity information provided by the navigation message is not desirable for real-time applications as the ground control segment (GCS) requires a few hours to broadcast a failure [37]. Hence, integrity monitoring is usually obtained by means of additional frameworks. These frameworks include external sensor fusion-based techniques as well as internal techniques. Sensor fusion techniques leverage onboard navigation sensors to monitor the navigation solution, while internal techniques typically use the redundant information within the transmitted navigation signals for this purpose. In [17], a method was proposed to leverage lidar measurements to improve both the integrity of the navigation solution and the fault detection capabilities. The proposed method employed an unscented Kalman filter (UKF) to fuse Lidar and GPS data. Then, an algorithm was described to extract the lidar odometry covariance to construct the RAIM test statistic. Considering the fact that the urban structures and tall buildings, which block GNSS signals, are rich with features detectable by lidar, this method was shown to be very effective for urban environment integrity monitoring. In [38], a method to incorporate an INS for fault detection was proposed. This method, employed an extended Kalman filter (EKF) to fuse INS and GPS measurements. Then, a sliding window estimator was formulated that solves the full-nonlinear maximum *a posteriori* estimate in real-time. Finally, the resulting window of residuals was used to implement an improved fault detection strategy, which is robust against EKF linearization errors. In [39], a method to combine GNSS, lidar, and inertial measurement unit (IMU) was proposed that calculates the integrity measures by analyzing the lidar return light intensity.

Finally, [8] proposed a method that incorporate data from camera and map-matching for both positioning and calculating the integrity of the navigation solution. In contrast to external integrity monitoring methods, RAIM alleviates the need for costly, bulky, and computationally intensive infrastructures.

Over the past few decades, a multitude of algorithms for RAIM have been introduced, including RAIM for GPS-only and multi-constellation GNSS frameworks. With the expected increase in the number of pseudorange sources, new RAIM methods have been studied to exploit the pseudoranges made on different GNSS satellites. Two of the existing algorithms include least-squares (LS) RAIM and multiple hypothesis solution separation (MHSS).

- **LS RAIM algorithm:** LS RAIM considers two scenarios for each satellite: fault-free and faulty operation. In the faulty case, a bias is added in one of the measurements. Since the position error is not directly observable, LS RAIM employs a residual-based test statistic to evaluate the consistency of pseudorange measurements. Fault detection is achieved by comparing the test statistic against a threshold [12]. Initially, the LS RAIM algorithm relied on the assumption that only one failure occurs at a time [11]. Later on, more sophisticated LS RAIM-based algorithms were developed to account for simultaneous faults [40], [41]. In [14], the performance of LS RAIM for combined Galileo-GPS was evaluated. Another variation of the LS RAIM is known as forward-backward (FB) RAIM. FB RAIM is similar to the LS RAIM in its core and consists of two phases: forward and backward. The forward phase includes four tests: (i) geometry preliminary check, (ii) global test to check the measurements' consistency, (iii) local test to identify the outlier, and (iv) separability test to check the measurements' correlation. The backward phase includes a global test to re-introduce the erroneously-rejected measurements. FB RAIM was shown to be a robust algorithm for multi-constellation frameworks. In [42], GPS-Galileo FB RAIM was investigated in a signal-degraded environments. An initial study on the differential SOP system (where a baseline between the base and rover is present) was conducted in [43], where the reduction in the PL was analyzed. This paper differs from [43] trough the following. First, in this paper, the terrestrial pseudoranges are directly injected into the estimator alongside GNSS pseudoranges. With the differential SOP system, the base and rover were making pseudorange measurements to the same SOP transmitters, while the rover had no access to GNSS signals. Second, [43] assumed the presence of a stationary agent in the navigator's environment, referred to as the base, which has knowledge of its own state at all time. The base's purpose was to estimate the dynamic stochastic clock errors of SOP transmitters and to share these estimates with the navigator. It was assumed that the base had direct line-of-sight (LOS) to all SOP towers. This assumption may not be practical in the real-world. Therefore, developing a self-contained solution is desirable. To this end, this paper develops a self-contained UAV navigation framework that fuses GNSS and SOP pseudoranges, to simultaneously localize the UAV-mounted receiver and estimate the receiver's and transmitters' clock errors.
- **MHSS algorithm:** The MHSS algorithm, was first introduced in [44] and [45]. MHSS constructs a fault tree, which refers to a set of assumptions about the environment in which a RAIM algorithm is applied. The measurements are supposed to be in one out of a set of different branches of the fault tree, to each of which an *a priori* probability of occurrence is assigned. MHSS evaluates the different fault modes given the specified probabilities of fault and determines the optimal probability of missed detection for each mode. MHSS considers the potential usage of multi-constellation GNSS observations and is designed to account for multiple faults [46], [47]. In [14] and [15], MHSS was employed to study the integrity of GPS-Galileo and GPS-GLONASS multi-constellation frameworks, respectively.

As mentioned above, all RAIM algorithms employ a preliminary check to verify the geometry conditions. Favorable geometric conditions significantly enhances the capabilities of integrity monitoring processes. The notion of incorporating more measurements from GNSS augmentation systems (GBAS and SBAS) has been investigated in the literature [48]–[52]. More recently, it was demonstrated in [53] that GNSS-based VPL and HPL were reduced by 57% and 65%, respectively, when GBAS corrections were used. Instead of using dedicated GBAS and SBAS infrastructure, this paper proposes a combined GNSS-SOP RAIM and aims to investigate the improvement in the transmitters' geometry by incorporating terrestrial SOPs. SOP towers are more abundant than dedicated infrastructure and are freely available. Also, SOPs are not limited to airport vicinities; hence, UAVs navigating in urban environments could benefit from SOPs' transmitted signals. Moreover, in contrast to satellites, terrestrial SOPs inherently transmit at low elevation angles. What is more, UAVs typically fly above terrestrial SOPs, enabling reception from negative elevation angles. As a result, a significant improvement in the geometry is expected by adding terrestrial SOP measurements. This paper, first, studies the SOP pseudorange characterization. This allows different assumptions to be placed on GNSS-SOP RAIM. Next, this paper evaluates the performance of the proposed GNSS-SOP RAIM from a PL standpoint.

III. NAVIGATION FRAMEWORK

This section formulates a weighted nonlinear least-squares (WNLS)-based framework for standalone UAV navigation with GNSS-SOP measurements. The navigation environment comprises a UAV, N SOP towers, and M GNSS satellites. The SOP towers are assumed to be stationary with known 3-dimensional (3-D) positions. This assumption implicitly places stringent requirements on a database integrity. In practice, one could map the SOP transmitter via several approaches, such as radio mapping or satellite images and store them in a local and/or cloud-hosted database, which is continuously maintained. This has been the subject of prior research [54], [55]. It was shown that the location of the SOPs can be mapped *a priori* using one method or a combination of several methods from the list below:

- Extracting from satellite imagery, such as Google database [56].
- Extracting from publicly available database [57].
- Estimating according to the frameworks presented in [55], [58].

The UAV is equipped with a GNSS receiver that makes pseudorange measurements to GNSS satellites at discrete-time instants $k = 0, 1, \ldots$, according to

$$z'_{\text{GNSS}_m}(k) = \left\| \boldsymbol{r}_r(k) - \boldsymbol{r}_{\text{GNSS}_m}(k) \right\|_2 + c \cdot \left[\delta t_r(k) - \delta t_{\text{GNSS}_m}(k) \right] + v_{\text{GNSS}_m}(k),$$

where $z'_{\text{GNSS}_m} \triangleq z_{\text{GNSS}_m} - c \cdot \delta t_{\text{iono}} - c \cdot \delta t_{\text{tropo}}$; δt_{iono} and δt_{tropo} are the known ionospheric and tropospheric delays, respectively; c is the speed of light; $\boldsymbol{r}_{\text{GNSS}_m}$ and δt_{GNSS_m} are the position and clock bias of the m-th GNSS satellite, respectively; and $\boldsymbol{r}_r \triangleq [x_r,\ y_r,\ z_r]^{\mathsf{T}}$ and δt_r are the receiver's position and clock bias, respectively. The term v_{GNSS_m} is the m-th GNSS satellite measurement noise, which is modeled as a zero-mean white Gaussian random sequence with variance $\sigma^2_{\text{GNSS}_m}$.

The UAV is also equipped with an SOP receiver that makes pseudorange measurements to terrestrial SOPs. A model of the pseudorange measurement, after mild approximations discussed in [59], is given by

$$z_{\text{SOP}_n}(k) = \left\| \boldsymbol{r}_r(k) - \boldsymbol{r}_{\text{SOP}_n} \right\|_2 + c \cdot \left[\delta t_r(k) - \delta t_{\text{SOP}_n}(k) \right] + v_{\text{SOP}_n}(k),$$

where $\boldsymbol{r}_{\text{SOP}_n}$ and δt_{SOP_n} are the position and clock bias of the n-th SOP transmitter, respectively, and v_{SOP_n} is the n-th SOP measurement noise, which is modeled as a zero-mean white Gaussian random sequence with variance $\sigma^2_{\text{SOP}_n}$.

The UAV estimates its state vector $\boldsymbol{x}_r \triangleq \left[\boldsymbol{r}_r{}^{\mathsf{T}}, c\delta t_r \right]^{\mathsf{T}}$ by fusing these measurements using a WNLS estimator. The clock biases $\{\delta t_{\text{SOP}_n}\}_{n=1}^{N}$ are modeled as first-order polynomials, i.e., $\delta t_{\text{SOP}_n}(k) \approx \dot{\delta t}_{\text{SOP}_n} kT + \delta t_{\text{SOP}_{n,0}}$, where $\dot{\delta t}_{\text{SOP}_n}$ is the constant clock drift of the n-th transmitter, $\delta t_{\text{SOP}_{n,0}}$ is the corresponding initial bias, T is the sampling time, and k is the time-step. The parameters of the first-order polynomials, i.e., $\delta t_{\text{SOP}_{n,0}}$ and $\dot{\delta t}_{\text{SOP}_n}$, can be transmitted to the user from a ground-based station, or can be calculated by the UAV itself from GNSS data and the measured pseudoranges using a LS estimator according to the method described in [60]. Note that $\delta t_{\text{SOP}_{n,0}}$ and $\dot{\delta t}_{\text{SOP}_n}$ can be assumed as constant parameters; therefore, the UAV does not need to employ a Kalman filter (KF) to continuously estimate them over time. More details about the first-order polynomial model of the SOP clock bias is discussed in [43], [61]. The impact of model mismatch due to using the first-order polynomial model on the measurement accuracy is discussed in Subsection VI-E.

Subsequently, the vector of all measurements given by

$$\boldsymbol{z} \triangleq \left[z'_{\text{GNSS}_1}, \ldots, z'_{\text{GNSS}_M}, z_{\text{SOP}_1}, \ldots, z_{\text{SOP}_N} \right]^{\mathsf{T}},$$

The UAV-mounted receiver's state vector is estimated using WNLS. The model is linearized according to

$$\Delta \boldsymbol{z} = \mathbf{H}\, \Delta \boldsymbol{x}_r + \boldsymbol{v},$$

where $\Delta \boldsymbol{z} \triangleq \boldsymbol{z} - \hat{\boldsymbol{z}}$ is the difference between the measurement vector $\boldsymbol{z}$ and its estimate $\hat{\boldsymbol{z}}$, $\Delta \boldsymbol{x}_r \triangleq \boldsymbol{x}_r - \hat{\boldsymbol{x}}_r$ is the difference between the receivers's state vector $\boldsymbol{x}_r$ and its estimate $\hat{\boldsymbol{x}}_r$, and $\boldsymbol{v} \triangleq \left[v_{\text{GNSS}_1}, \ldots, v_{\text{GNSS}_M}, v_{\text{SOP}_1}, \ldots, v_{\text{SOP}_N} \right]^{\mathsf{T}}$. The measurement Jacobian used in the WNLS estimator is $\mathbf{H} = \left[\mathbf{H}^{\mathsf{T}}_{\text{GNSS}}, \mathbf{H}^{\mathsf{T}}_{\text{SOP}} \right]^{\mathsf{T}}$, where $\mathbf{H}_{\text{GNSS}}$ and $\mathbf{H}_{\text{SOP}}$, shown at the bottom of the page, where $\mathsf{c}(\cdot)$ and $\mathsf{s}(\cdot)$ denote the cosine and sine functions, respectively; el_{GNSS_m} and az_{GNSS_m} are the elevation and azimuth angles of the m-th GNSS satellites, respectively; and el_{SOP_n} and az_{SOP_n} are the elevation and azimuth angles of the n-th SOP transmitter, respectively. All elevation and azimuth angles are expressed in the East, North, Up (ENU) local coordinate frame, centered at the receiver's position. The weighting matrix in the WNLS is chosen as the inverse of the measurement noise covariance

$$\mathbf{R} = \text{diag}\left[\sigma^2_{\text{GNSS}_1}, \ldots, \sigma^2_{\text{GNSS}_M}, \sigma^2_{\text{SOP}_1}, \ldots, \sigma^2_{\text{SOP}_N} \right],$$

where diag$(\cdot)$ denotes a diagonal matrix.

$$\mathbf{H}_{\text{GNSS}} \triangleq \begin{bmatrix} -\mathsf{c}(el_{\text{GNSS}_1})\mathsf{s}(az_{\text{GNSS}_1}) & -\mathsf{c}(el_{\text{GNSS}_1})\mathsf{c}(az_{\text{GNSS}_1}) & -\mathsf{s}(el_{\text{GNSS}_1}) & 1 \\ \vdots & \vdots & \vdots & \vdots \\ -\mathsf{c}(el_{\text{GPS}_M})\mathsf{s}(az_{\text{GPS}_M}) & -\mathsf{c}(el_{\text{GPS}_M})\mathsf{c}(az_{\text{GPS}_M}) & -\mathsf{s}(el_{\text{GPS}_M}) & 1 \end{bmatrix}$$

$$\mathbf{H}_{\text{SOP}} \triangleq \begin{bmatrix} -\mathsf{c}(el_{\text{SOP}_1})\mathsf{s}(az_{\text{SOP}_1}) & -\mathsf{c}(el_{\text{SOP}_1})\mathsf{c}(az_{\text{SOP}_1}) & -\mathsf{s}(el_{\text{SOP}_1}) & 1 \\ \vdots & \vdots & \vdots & \vdots \\ -\mathsf{c}(el_{\text{SOP}_N})\mathsf{s}(az_{\text{SOP}_N}) & -\mathsf{c}(el_{\text{SOP}_N})\mathsf{c}(az_{\text{SOP}_N}) & -\mathsf{s}(el_{\text{SOP}_N}) & 1 \end{bmatrix},$$

TABLE I
CHARACTERISTICS OF RECORDED CELLULAR SOPS

Environment	Platform	Number of towers	Signal type	Freq. [MHz]	Bandwidth [MHz]	Length [s]	Date [DD/MM/YYYY]
Open sky	Stationary	2	LTE	2125 and 1955	20	–	13/5/2019
Semi-urban and urban	GV	2	LTE	2145 and 1955	20	1500	15/11/2016
	GV	3	LTE	2145 and 1955	20	2000	20/1/2017
	GV	4	LTE	2145 and 739	20 and 10	1600	22/6/2018
	GV	5	LTE	1955 and 739	20 and 10	580	27/6/2016
	GV	3	LTE	739	10	825	5/11/2017
	GV	5	LTE	1955 and 739	20 and 10	1800	22/8/2018
Deep Urban	GV	2	LTE	2145 and 1955	20	345	12/10/2018
	GV	2	LTE	2145 and 1955	20	500	24/8/2018
Open sky and Semi-urban	UAV	2	CDMA	882.75	1.23	3300	13/5/2017
	UAV	7	CDMA	882.75	1.23	2900	22/2/2017
	UAV	8	CDMA	882.75	1.23	2200	1/10/2017
	UAV	8	CDMA	882.75	1.23	2600	1/10/2017
	UAV	2	CDMA	882.75	1.23	3500	15/11/2017
Urban	UAV	11	LTE	739, 1955, 2125, and 2145	10	605	16/6/2019

IV. SOP PSEUDORANGE ERROR CHARACTERIZATION

In order to incorporate SOP measurements into a RAIM-type framework and determine the integrity of the combined SOP-GNSS system, one must statistically characterize SOP pseudorange measurements, namely determine their accuracy and failure rates. While recent research have studied fault and error sources in SOP-based navigation [43], this paper is focuses on the statistical properties of these resulting errors. In this paper, the data collected by the Autonomous Systems Perception, Intelligence, and Navigation (ASPIN) Laboratory over several years of experimental campaigns was used to characterize the statistics of cellular SOP pseudorange measurements. Cellular SOP pseudoranges were recorded with UAVs for an aggregate of several hours of flights. These pseudoranges were obtained using the Multichannel Adaptive TRansceiver Information eXtractor (MATRIX) [62] software-defined receiver (SDR) in (i) different environments; (ii) at different carrier frequencies; and (iii) for different signal types, including long-term evolution (LTE) and code-division multiple access (CDMA) signals. In order to perform these experiments in different environmental conditions, the data collection was carried out in California, USA: Riverside (open sky), San Bernardino (semi-urban), Aliso Viejo (urban), and Riverside (deep urban). While this paper tries to characterize the impact of the most well-known SOP error sources, such as multipath, clock model mismatch, poor geometric configuration, etc., accounting for all possible sources of errors (e.g., software bugs, communication drops, hardware failure, etc.) requires continuous data collection for thousands of hours, which is considered for future work. The characteristics of the recorded data are tabulated in Table I. As expected, the quality of these measurements is highly dependent on the environment. Note that the data collected by ground vehicles (GVs) was used to characterize cellular SOP measurements, mimicking UAVs flying at low altitudes (e.g., during takeoff and landing phases and performing missions such as goods delivery).

Note that the method that was used in this paper to characterize the SOP pseudorange error was DeCleene's single cdf-overbounding approach. Generally, an overbounding approach considers the worst-case scenario, given the stored data available in the database. Because of this, it is acceptable to apply DeCleene algorithm on the recorded data in post-processing and then, update the overbounding cdf's parameteres in the database, from which the navigator can pull these parameters. This can be achieved in post-process or in real-time. Next, the pseudorange measurements' errors were characterized using the method discussed in [36] via the following three steps.

- **Step 1:** The true ranges between the receiver and SOP transmitter (i.e., $\left\|\boldsymbol{r}_r(k) - \boldsymbol{r}_{\text{SOP}_n}(k)\right\|_2$) are removed from the recorded pseudoranges $z_{\text{SOP}_n}(k)$. The true ranges are known *a priori* from the knowledge of the transmitters' location and receiver's ground truth position. The resulting measurement after removing the true range is given by:

$$\begin{aligned} z'_{\text{SOP}_n}(k) &\triangleq z_{\text{SOP}_n}(k) - \left\|\boldsymbol{r}_r(k) - \boldsymbol{r}_{\text{SOP}_n}(k)\right\|_2 \\ &= c \cdot \left[\delta t_r(k) - \delta t_{\text{SOP}_n}(k)\right] + v_{\text{SOP}_n}(k). \end{aligned}$$

- **Step 2:** The error term due to the difference between the receiver's and the transmitter's clock biases (i.e., $c \cdot \left[\delta t_r(k) - \delta t_{\text{SOP}_n}(k)\right]$) is removed from the measurement $z'_{\text{SOP}_n}(k)$. To this end, a first-order polynomial approximation with a constant initial clock bias $c\delta t_{\text{r},\text{SOP}_{n,0}}$ and drift $c\dot{\delta t}_{\text{r},\text{SOP}_{n,0}}$ is used to model the difference

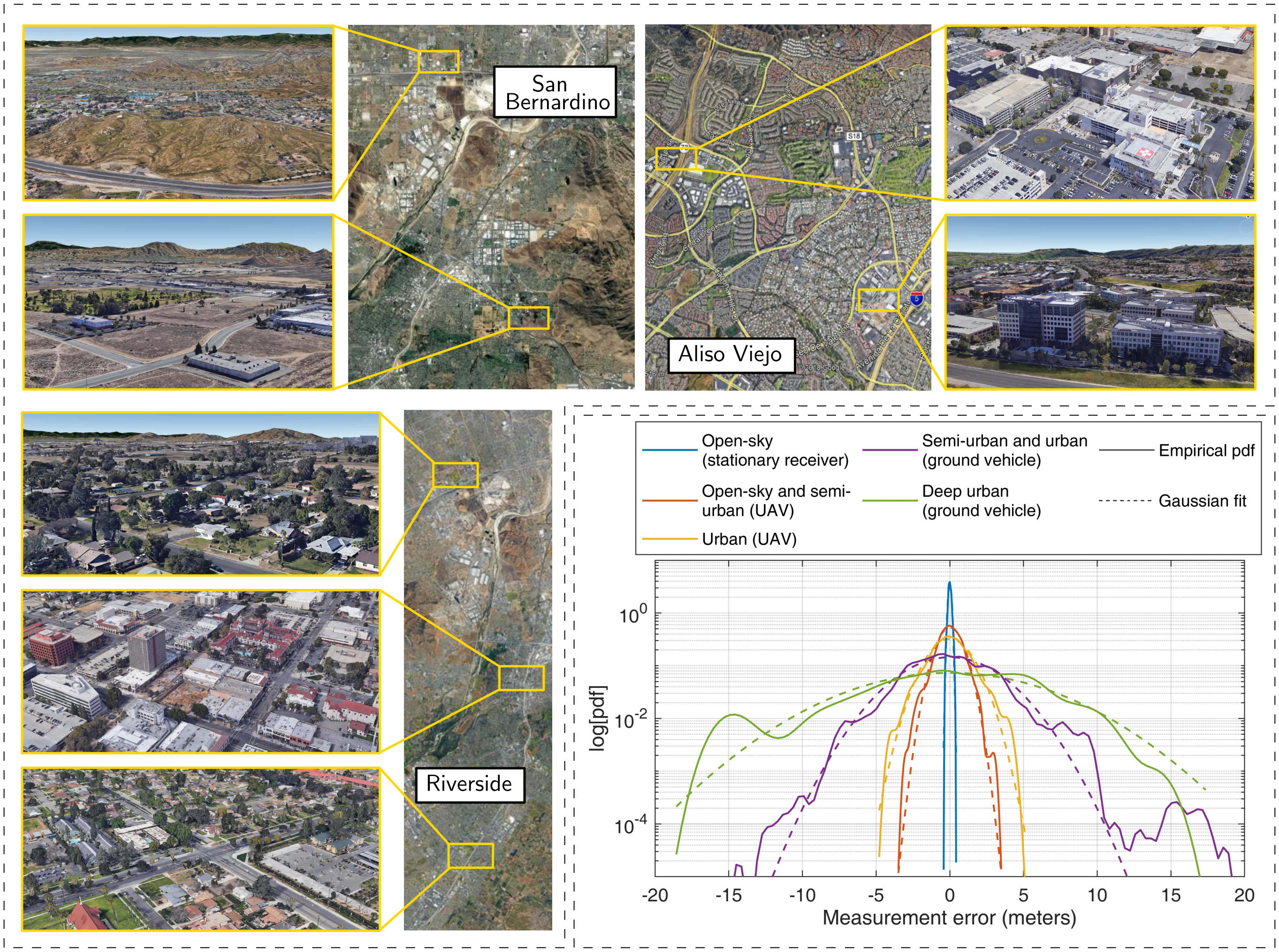

Fig. 2. Characterization of cellular SOP pseudoranges: SOPs environments in different locales in California, USA and corresponding pdfs.

between the receiver's and transmitter's clock biases, i.e.,

$$c\cdot\left[\delta t_r(k)-\delta t_{\text{SOP}_n}(k)\right]=c\dot{\delta t}_{\text{r},\text{SOP}_{n,0}}\,kT+c\delta t_{\text{r},\text{SOP}_{n,0}}.$$

The constants $c\dot{\delta t}_{\text{r},\text{SOP}_{n,0}}$ and $c\delta t_{\text{r},\text{SOP}_{n,0}}$ are estimated by post-processing the recorded data from time-step 0 to time-step K via an LS estimator, which minimizes the cost function $\mathbf{G}$ given by

$$\mathbf{G}\triangleq\left\|\boldsymbol{y}-\mathbf{S}\begin{bmatrix}c\dot{\delta t}_{\text{r},\text{SOP}_{n,0}}\\ c\delta t_{\text{r},\text{SOP}_{n,0}}\end{bmatrix}\right\|_2^2,$$

$$\mathbf{S}\triangleq\begin{bmatrix}0 & T & \ldots & KT\\ 1 & 1 & \ldots & 1\end{bmatrix}^{\mathsf{T}},$$

where the LS observation vector $\boldsymbol{y}$ is given by

$$\boldsymbol{y}\triangleq\left[z'_{\text{SOP}_n}(0),\ldots,z'_{\text{SOP}_n}(K)\right]^{\mathsf{T}}.$$

The resulting measurement after removing the error due to clock bias difference is given by:

$$\begin{aligned}z''_{\text{SOP}_n}(k)&\triangleq z'_{\text{SOP}_n}(k)-c\dot{\delta t}_{\text{r},\text{SOP}_{n,0}}\,kT-c\delta t_{\text{r},\text{SOP}_{n,0}}\\&\simeq v_{\text{SOP}_n}(k).\end{aligned}$$

Although using the first-order polynomial approximation for modeling the SOP clock has been thoroughly studied in the literature [60], [61], this approximation may introduce faults that are not monitored. In Subsection VI-E, the effect of model mismatch in the aforementioned clock model on the measurement error is analyzed.

- **Step 3:** The sample mean and sample variance of the measurement error's pdf are calculated from

$$\hat{\mu}_{\text{SOP}_n}=\frac{1}{K+1}\sum_{k=0}^{K}z''_{\text{SOP}_n}(k),$$

$$\hat{\sigma}^2_{\text{SOP}_n}=\frac{1}{K}\sum_{k=0}^{K}\left[z''_{\text{SOP}_n}(k)-\hat{\mu}_{\text{SOP}_n}\right]^2.$$

Fig. 2 illustrates the empirical pdfs found from the collected measurements. Overlayed on these pdfs are the Gaussian pdf fits with the calculated sample mean $\hat{\mu}_{\text{pdf,sample}}$ and sample variance $\hat{\sigma}_{\text{pdf,sample}}$ over all SOPs. Table II summarizes $\hat{\mu}_{\text{pdf,sample}}$ and $\hat{\sigma}_{\text{pdf,sample}}$ in different environments. Note that the calculated sample means are almost zero due to **Step 2** described above.

With respect to integrity, an overbounding function is conservative if it predicts the occurrence of large navigation errors to be at least as frequent as their actual occurrence [13]. Since both the empirical and overbound plots in Fig. 2 are pdfs and

TABLE II

SAMPLE MEAN ($\hat{\mu}_{\text{pdf,sample}}$) AND SAMPLE VARIANCE ($\hat{\sigma}_{\text{pdf,sample}}$) OF GAUSSIAN PDFS OF PSEUDORANGE MEASUREMENT ERROR IN DIFFERENT ENVIRONMENTS

Altitude	**Environment**	$\hat{\mu}_{\text{pdf,sample}}$	$\hat{\sigma}_{\text{pdf,sample}}$
–	Open sky	1.41×10^{-15} m	0.11 m
Low altitude	Urban and semi-urban	-1.24×10^{-16} m	2.74 m
	Deep urban	-1.05×10^{-15} m	5.42 m
High altitude	Semi-urban	-3.66×10^{-18} m	0.75 m
	Urban	7.10×10^{-18} m	1.32 m

TABLE III

SINGLE-CDF APPROACH-BASED ($\hat{\mu}_{\text{cdf,overbound}}$) AND SAMPLE VARIANCE ($\hat{\sigma}_{\text{cdf,overbound}}$) OF GAUSSIAN CDFS OF PSEUDORANGE MEASUREMENT ERROR IN DIFFERENT ENVIRONMENTS

Altitude	**Environment**	$\hat{\mu}_{\text{cdf,overbound}}$	$\hat{\sigma}_{\text{cdf,overbound}}$
–	Open sky	0 m	0.22 m
Low altitude	Urban and semi-urban	0 m	3.02 m
	Deep urban	0 m	5.97 m
High altitude	Semi-urban	0 m	0.97 m
	Urban	0 m	2.64 m

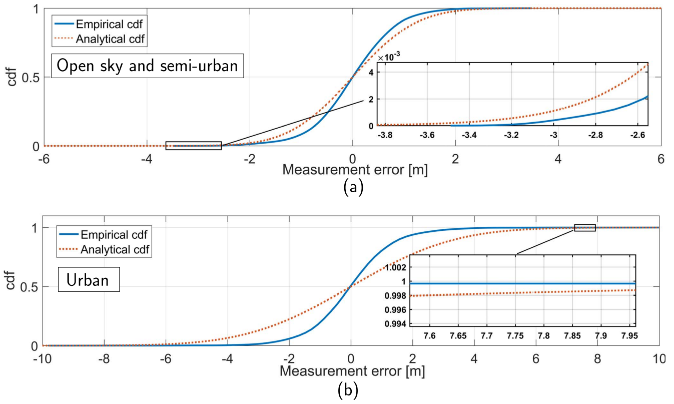

(a)

(b)

Fig. 3. Characterization of cellular SOP pseudorange measurement accuracy in different environments in which the pseudoranges were collected. Empirical cdf of pseudorange errors and analytical Gaussian cdfs obtained from a single-cdf approach are illustrated for each environment: (a) Open sky and semi-urban and (b) urban.

integrate to one, it is not possible for the pdf overbound to hold for all values of the empirical pdf. In fact, there exists small residuals around the tails, which are not necessarily characterized by a Gaussian distribution. Since the integrity requirements impose constraints at 10^{-7} level, this aspect needs to be analyzed further, validating that the integrity risk is ensured, especially around the tails. Over the past few years, different bounding strategies have been investigated in the literature to construct conservative bounds, which represent the empirical measurement error. The first overbounding approach that successfully provided conservative bounds for the empirical measurement error was DeCleene's single cdf-overbounding approach [63]. In [63], it was proven that the assumption for a zero-mean Gaussian error distribution can be replaced by a requirement that the error distribution is symmetric, unimodal, and whose cdf is bounded by a Gaussian error distribution overbounded for errors less than the mean and underbounded for errors greater than the mean, i.e.,

$$G_o > G_a, \quad G_a \leq 0.5$$
$$G_o \leq G_a, \quad G_a > 0.5,$$

where G_o and G_a are the overbound cdf and the empirical cdf, respectively. To ensure the integrity risk around the tails, the single-cdf overbounding method [63] was implemented. Fig. 3 illustrates the empirical cdfs found from the collected measurements. Overlayed on these cdfs are the cdf overbounds obtained from DeCleene's single cdf-overbounding approach. Table III summarizes $\hat{\mu}_{\text{cdf,overbound}}$ and $\hat{\sigma}_{\text{cdf,overbound}}$ in different environments. As it can be seen from Fig. 3, the integrity is ensured over all empirical measurement errors. Therefore, DeCleene's single cdf-overbounding method was used in this paper during simulations and real-world experiments.

Calculating the SOP measurements' fault rate is a more challenging problem as no official SOP measurement integrity standard has been issued yet. According to the Air Force GPS Standard Positioning Service Performance Standard (SPS PS) [64], the GPS measurement fault is defined by an error greater than 4.42 times the broadcast User Range Accuracy (URA). However, this cannot directly apply to SOP measurements. On one hand, URA cannot be assessed from the measurements and the user needs to receive this parameter from external entities, which ensure the integrity level. On the other hand, the SOP navigation message does not include URA information. The lack of SOP integrity information is analogous to the lack of GLONASS integrity information over the first years of operation, where no URA data was available in the GLONASS's Receiver Independent Exchange Format (RINEX) file. Using the methods that evaluate the GLONASS fault rate without having access to the broadcast URA [15], [65], the SOP fault rate can be approximated. It is first important to establish the type of operating environment. In this paper low-altitude UAV navigation in urban/deep urban environments is considered. One can see from Fig. 2 that the pseudorange error in these environments does not exceed 19.12 m (solid purple curve). Therefore, it is reasonable to consider an induced bias larger than 20 m as a fault. Table III shows that $\hat{\sigma}_{\text{cdf,overbound}} = 5.97$ m for a low-altitude UAV in an urban/deep urban environment. Consequently, the 20 m fault threshold corresponds to 3.35 times the standard deviation of the overbound cdf, which in turn implies that the probability of a cellular SOP transmitter being in a faulty state is 8.08×10^{-4}. The approximated fault bias and the corresponding probability are demonstrated in Fig. 4. It is important to note that the reliability of cellular SOPs has not yet been fully characterized. This is a tedious process that requires thousands of hours of data collection. The SOP integrity parameters obtained in this paper are still preliminary and used as a proof of concept. As the database of collected SOP data grows, these parameters can be further refined. The

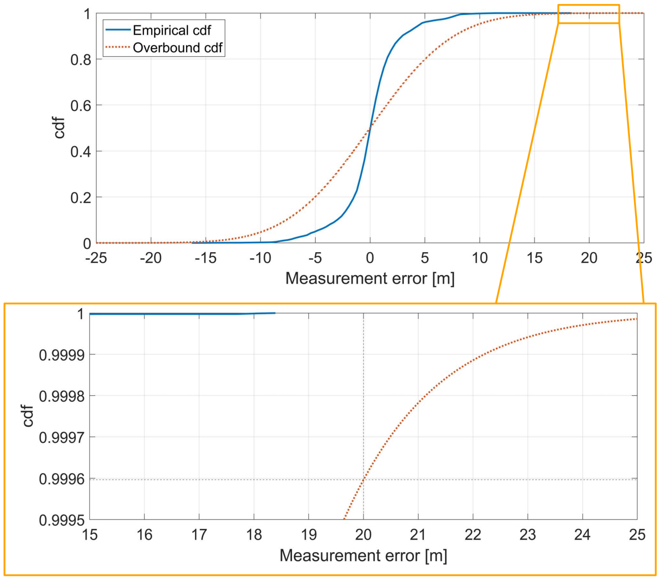

Fig. 4. The approximated fault bias and its corresponding probability. A fault bias of 20 m in magnitude corresponds to an 8.08×10^{-4} fault probability.

aim of this paper is to present a methodology to calculate these parameters and how to use them for UAV integrity monitoring. As such, an 8.08×10^{-4} fault probability could be either conservative or optimistic. However, in the case of the latter, it has been shown in [66] that incorporating SOPs would still yield improvement over GPS-only for high and unlikely SOP fault probabilities of 10^{-2}.

V. PL REDUCTION VIA ADDING SOPS

RAIM algorithms provide the user with an estimate of the confidence in the position information via PL. Several methods to calculate PL have been proposed in the literature. This paper considers the MHSS-based PL presented in [67], [68] to study the effect of adding SOPs into the transmitter-to-receiver geometry. Formulating other types of RAIM for other SOP-GNSS navigation frameworks is similar and could be investigated in future work. The associated VPL and HPL under fault-free hypothesis are obtained from

$$\begin{aligned}
\mathrm{VPL} &= K_v\, d_{\mathrm{UP}}, \quad d_{\mathrm{UP}} = \sqrt{\sum_{i=1}^{M+N} \mathbf{S}^2{}_{3,i}\, \mathbf{R}_{i,i}}, \\
\mathrm{HPL} &= K_h d_{\mathrm{H}}, \quad d_{\mathrm{H}}^2 = \frac{{d_{\mathrm{E}}}^2 + {d_{\mathrm{N}}}^2}{2} \\
&\quad + \sqrt{\left(\frac{{d_{\mathrm{E}}}^2 - {d_{\mathrm{N}}}^2}{2}\right)^2 + {d_{\mathrm{EN}}}^2}, \\
d_{\mathrm{E}} &= \sqrt{\sum_{i=1}^{M+N} \mathbf{S}^2{}_{1,i}\, \mathbf{R}_{i,i}}, \quad d_{\mathrm{N}} = \sqrt{\sum_{i=1}^{M+N} \mathbf{S}^2{}_{2,i}\, \mathbf{R}_{i,i}}, \\
d_{\mathrm{EN}} &= \sqrt{\sum_{i=1}^{M+N} \mathbf{S}_{1,i} \mathbf{S}_{2,i}\, \mathbf{R}_{i,i}}, \qquad (1)
\end{aligned}$$

where $\mathbf{S} \triangleq \left(\mathbf{H}^{\mathsf{T}}\mathbf{R}^{-1}\mathbf{H}\right)^{-1}\mathbf{H}^{\mathsf{T}}\mathbf{R}^{-1}$ and $\mathbf{X}_{ij}$ denotes the element of i-th row and j-th column of a matrix $\mathbf{X}$. The coefficients K_v and K_h are defined according to

$$K_v \triangleq \Phi^{-1}(1 - \beta_v/2), \quad K_h \triangleq \Phi^{-1}(1 - \beta_h/2),$$

where Φ denotes the cdf of the standard Gaussian distribution and β_v and β_h are the integrity budget for the vertical and horizontal components, whose values are set to 9.8×10^{-8} and 2×10^{-9}, respectively. The risk under potential failure conditions can be evaluated by a faulted hypothesis. The PL for the faulted hypothesis is formulated in [68].

In contrast to the GNSS-only approaches, where the elevation range is limited between some elevation mask and 90 degrees, the proposed GNSS-SOP framework can double the elevation angle range to -90 to 90 degrees. This is due to the fact that UAVs can fly even above the terrestrial SOPs. It is important to note that the improvement in transmitter-to-receiver geometry is highly dependent on the initial configuration of the satellites to which the SOPs are added. For example, if no GNSS satellite at zenith is considered, the reduction obtained by adding a SOP will be much larger. In order to perform a fair comparison and to account for as many as possible satellite configurations, Monte Carlo simulations are adopted with 10^4 realizations, which is large enough to cover a variety of initial satellite configuration.

Next, the PL reduction by incorporating additional GNSS measurements versus additional SOP measurements is investigated as follows. In each Monte Carlo realization, M GNSS satellite azimuth and elevation angles were generated according to

$$\begin{aligned}
az_{\mathrm{GNSS}_m} &\sim \mathcal{U}(-180, 180), \quad m = 1, \ldots, M \\
el_{\mathrm{GNSS}_m} &\sim \mathcal{U}(el_{\mathrm{mask}}, 90), \quad m = 1, \ldots, M,
\end{aligned}$$

where $\mathcal{U}(a, b)$ is the uniform distribution over the interval $[a, b]$ and el_{mask} is a pre-defined elevation mask. Then, an additional measurement at el_{new} and az_{new} was generated according to

$$\begin{aligned}
az_{\mathrm{new}} &\sim \mathcal{U}(-180, 180), \\
el_{\mathrm{new}} &\in \{-90, -80, \ldots, 80, 90\}.
\end{aligned}$$

This model is equivalent to adding a new transmitter into a pre-deployed random set of transmitters, while the elevation angle of the new transmitter can be swept between -90 and 90 degrees. Next, The reduction in the PLs due to adding this new transmitter was recorded at each elevation angle between -90 and 90 degrees. The average and standard deviation of the corresponding PLs' reduction for introducing this additional transmitter at a sweeping elevation angle $-90 \leq el_{\mathrm{new}} \leq 90$ degrees is plotted in Fig. 5 for different values of the pre-deployed transmitters M and different elevation mask el_{mask}. The PLs are calculated using (1).

Fig. 5 clearly shows that while adding more measurements from other satellites decreases the PLs, measurements from transmitters at low elevation angles are more effective in minimizing the PL than transmitters at elevation angles between 0 and 90 degrees. Moreover, by comparing the solid lines and dashed lines from the same colors, it is evident that in the environment with high elevation mask (e.g., deep urban), the amount of reduction in the PL due to adding SOPs

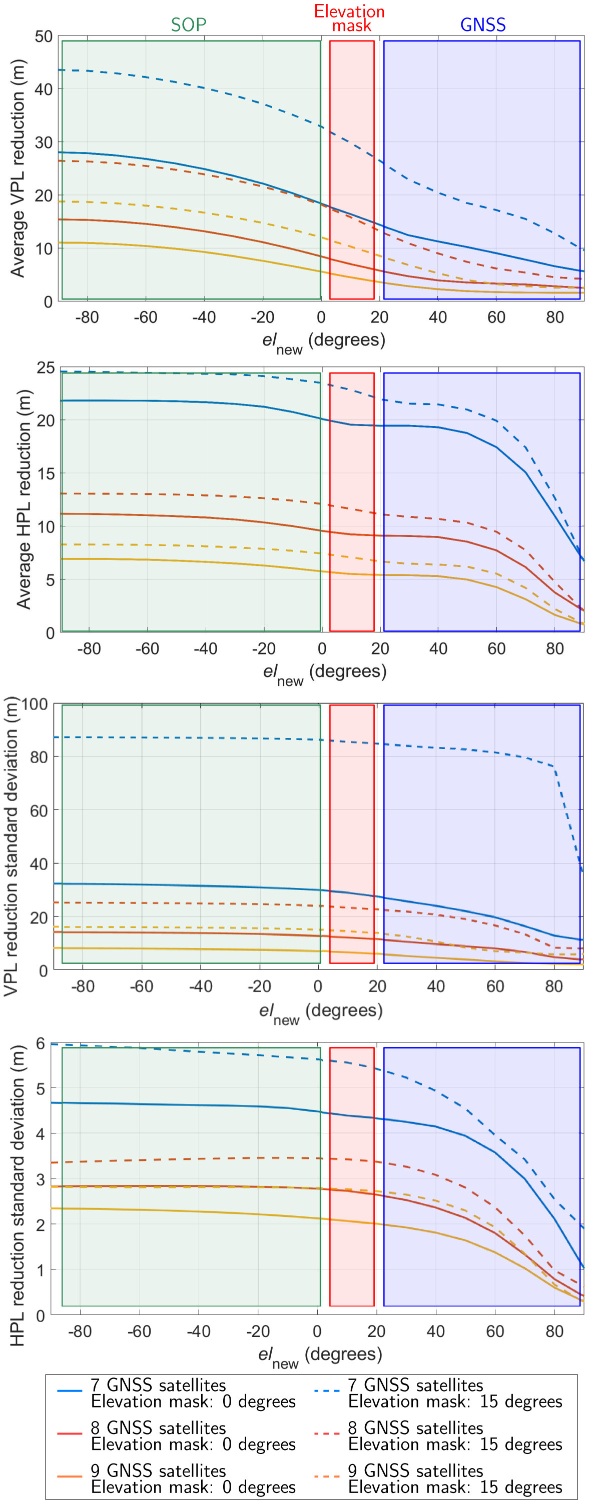

Fig. 5. The average and standard deviation of the reduction in VPL and HPL after adding an additional measurement at an elevation angle $-90 \leq el_{\text{new}} \leq 90$ degrees for $M = 7, \ldots, 9$ and elevation masks: 0 and 15 degrees. The initial values of the VPLs for $M = 7, \ldots, 9$ and elevation masks 0 degrees were 31.67 m, 18.79 m, and 14.31 m; and the initial values of the VPLs for $M = 7, \ldots, 9$ and elevation masks 15 degrees were 47.07, m 29.72 m, and 22.00 m, respectively. This shows the proposed method was able to reduce the VPLs by more than 50%.

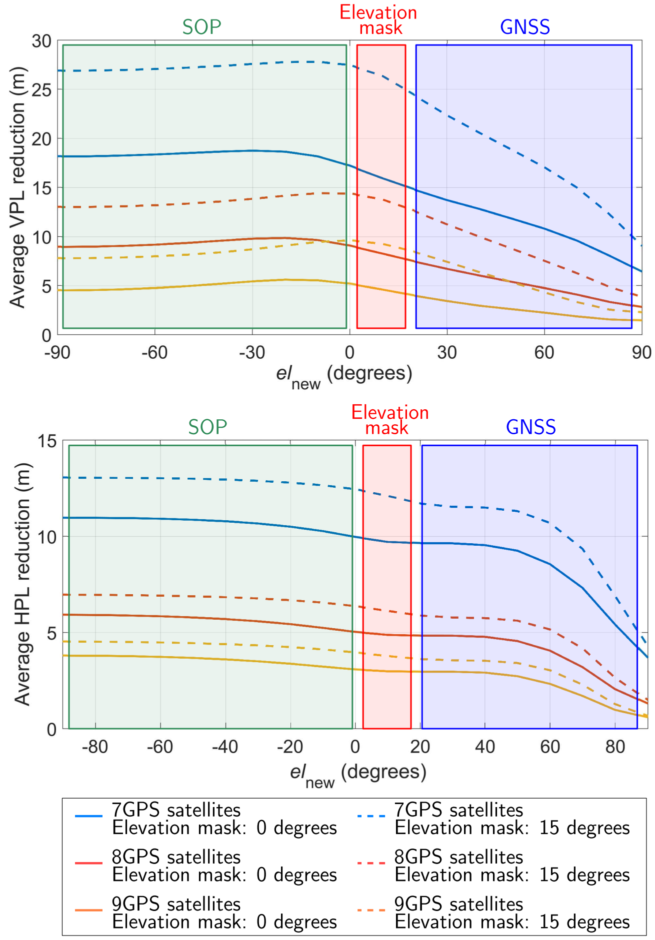

Fig. 6. The reduction in LS RAIM-based VPL and HPL after adding an additional measurement at an elevation angle $-90 \leq el_{\text{new}} \leq 90$ degrees for $M = 7, \ldots, 9$ and elevation masks: 0 and 15 degrees.

is significantly larger than the reduction in the PL due to adding satellites (specifically for VPL). Finally, the Monte Carlo-based analysis under same simulation conditions and data set was repeated for a VPL and a HPL constructed from LS RAIM. The results are shown in Fig. 6. As it can be seen, the results of the LS RAIM was similar to the MHSS-RAIM, which was demonstrated in Fig. 5.

VI. SIMULATION RESULTS

A simulation test was set up to evaluate the potential of exploiting SOPs for RAIM. To compare the PL of a GPS-only solution with that of a GPS-SOP solution, a stationary receiver at the Madrid Deep Space Communications Complex (MDSCC) was considered. The elevation and azimuth angles of the GPS satellite constellation above the receiver over a 24-hour period was computed using GPS ephemeris files collected at the MDSCC. To illustrate the PL reduction by incorporating SOP observations, 5 additional SOP transmitters were simulated at the test environment, and the resulting PL was evaluated. Throughout different simulations provided in this section, the number of SOP transmitters is fixed (5 SOPs) and their positions are listed in IV. However, in Subsection VI-D, the impact of the number of SOPs on the achieved PL is evaluated by varying the number of SOPs from 0 to 10. The simulation settings are given in Table IV. In Table IV, the UAV's and towers' positions are expressed in Geographic coordinate system.

TABLE IV
SIMULATION SETTINGS

Parameter	Definition	Value
$\{z_{\mathrm{GPS}_m}\}_{m=1}^{M}$	GPS pseudorange measurements	Extracted from the navigation RINEX file (20 July 2006 to 21 July 2006)
β_v	Integrity budget for the vertical component	9.8×10^{-8}
$\boldsymbol{r}_r$	UAV's position	$[40.429200, -4.249700, 900]$
N	Number of SOP transmitters	0-10
M	Number of GPS satellites	5 to 9
T	Sampling time	0.1 s
	SOP clock type	High-quality OCXO
	Receiver clock type	Typical OCXO
$\{\sigma_{\mathrm{GPS}_m}\}_{m=1}^{M}$	GPS measurement noise standard deviation	3 m
$\{\sigma_{\mathrm{SOP}_n}\}_{n=1}^{N}$	SOP measurement noise standard deviation	2 m
$\{\boldsymbol{r}_{\mathrm{SOP}_n}\}_{n=1}^{5}$	Towers' position	$[40.432549, -4.265973, 871]$ $[40.443643, -4.255776, 1089]$ $[40.438886, -4.243743, 806]$ $[40.430516, -4.228286, 778]$ $[40.421916, -4.248156, 766]$

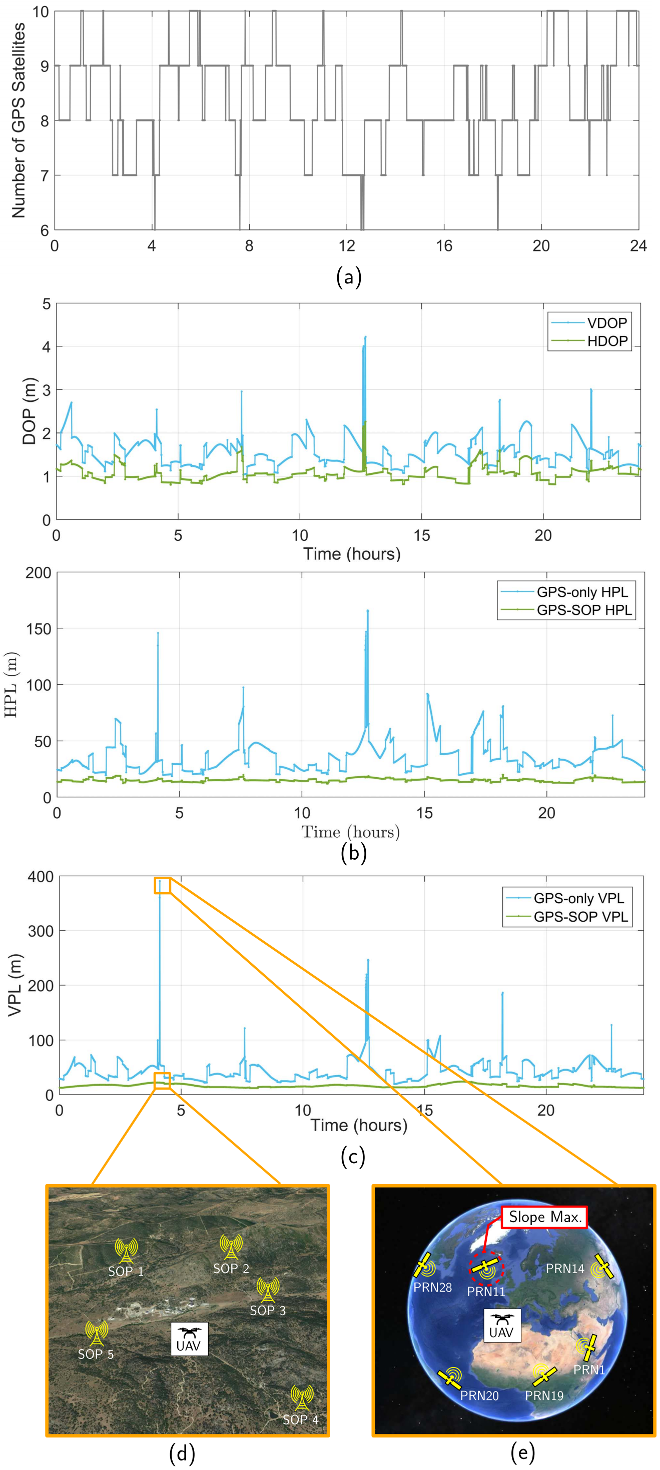

Fig. 7. Simulation environment and the simulation results: (a) The number of available GPS satellites for a 24-hour period. (b) The VDOP and HDOP of available GPS satellites for a 24-hour period, (c) Comparison between GPS-only and GPS-SOP PLs over 24 hours. (d) The simulation environment layout at Madrid Deep Space Communications Complex (MDSCC), the location of the receiver, and position of the SOP towers. (e) An instance where GPS-only VPL was 350 m due to poor satellite-to-receiver geometry.

A. PL Reduction via Adding SOPs

Fig. 7 (a) and (b) illustrates the associated number of available GPS satellites for a 24-hour period and the corresponding DOP metrics. Fig. 7 (c) illustrates the VPL and HPL obtained by the GPS-only solution (blue line) and the proposed GPS-SOP solution (green line). The average GPS-only VPL over 24 hours was 43.36 m, whereas the average GPS-SOP VPL was 16 m. Fig. 7 (c) also shows a few instances where the GPS-only VPL exceeds 200 m. By comparing Fig. 7 (a),(b) and Fig. 7 (c), it is evident that these instances correspond to poor satellite-to-receiver geometry, where the receiver had LOS to only 6 GPS satellites and VDOP is larger than 2.5. Fig. 7 (d) illustrates the simulation environment along with the location of the SOP towers. Fig. 7 (e) illustrates the GPS satellites configuration at a particular instance where the GPS-only VPL and HPL were around 350 m and 150 m, respectively. It can be seen that the PLs are significantly reduced in this instance by incorporating SOP transmitters.

B. Evaluating Different Elevation Masks

Next, the performance of the proposed framework for different elevation mask angles is evaluated. To this end, a simulation was conducted for elevation masks 0 to 23 degrees. The other simulation settings are the same as what has been tabulated in Table IV. In each run, GPS-only PLs and the proposed GPS-SOP PLs were calculated. The results are shown in Fig. 8. As can be seen, the GPS-only PLs were significantly increased by increasing the elevation mask, while the GPS-SOP PLs remained nearly constant. Hence, in the environment with large GPS elevation mask (e.g., deep urban

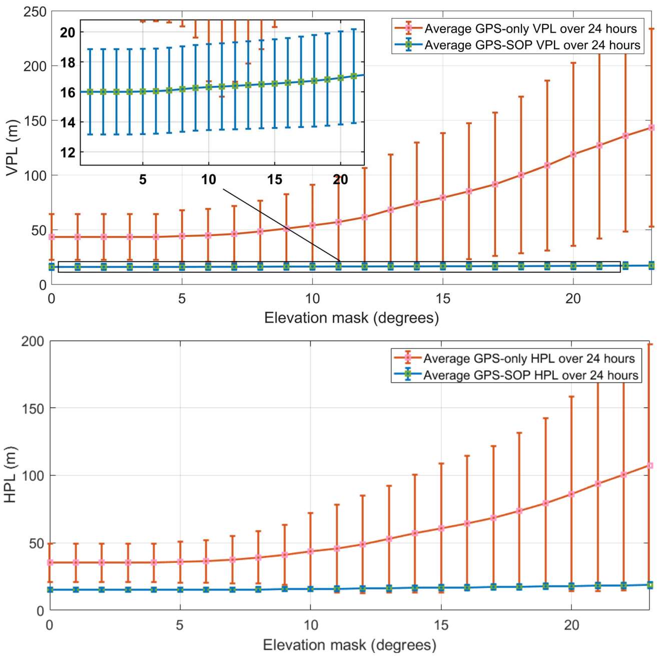

Fig. 8. Comparison between GPS-only PLs and the proposed GPS-SOP PLs for different elevation masks. As can be seen, the GPS-only PLs were significantly increased for large elevation masks, while the GPS-only PLs remained nearly constant. The vertical lines in top plot represent the error bar.

canyon), incorporating SOP measurements can effectively reduce the PLs.

C. Evaluating the Impact of SOP Configuration

This subsection, extends the analysis presented in Subsection VI-A to consider the geometries, which are poor from SOP configuration point of view. The statistics of cellular SOPs' configuration have been studied in the literature. In [69], it was shown that for cellular LTE SOPs, the distribution of the N transmitters' location can be modeled by a binomial point process (BPP) in an annular region $\mathbb{B}_o\left(d_{\min}, d_{\max}\right)$ where o is the origin, $d_{\min}$ is the far-field distance, and $d_{\max}$ is the maximum distance for which the receiver can reliably hear the SOPs (see Fig. 9(a)). Subsequently, the azimuth angles of the SOPs are uniformly distributed between 0 and 2π (see Fig. 9(b)). In [70], [71], it was demonstrated that terrestrial cellular SOPs as far as 3 km can be reliably acquired and tracked by UAVs. As such $d_{\max}$ is set to 3 km. It was also noted experimentally that $d_{\min}$ and can be approximated by 5 m.

The BPP model is used to evaluate the impact of the number of SOPs N on the performance of the proposed framework. To this end, the simulation with a setup presented in Subsection VI-A was conducted for $N = 0$ (GPS-only case) and $N = 1, 2, \ldots, 10$ (GPS-SOP case).

Throughout this test, the location of these 10 SOPs were fixed. Each of these 10 locations was generated using the BPP model. Then, for each of these cases, the simulation configuration tabulated in Table IV was applied and results were re-generated over 24 hours period. Finally, the average of the observed PLs were calculated. The results are shown in Fig. 10. The following can be concluded from this simulation. First, with $N = 1$, the proposed approach achieved an average VPL of 28 m compared to an average VPL of 43.36 m with the GPS-only case ($N = 0$). This shows that even adding one SOP transmitter can significantly reduce the VPL (same conclusion holds for HPL). Second, the results demonstrate the expected behavior that exploiting more SOPs yields higher PL reduction. However, the PL reduction is nearly constant after adding 6 or more SOPs. Third, as can be seen from Fig. 10, SOPs will not contribute negatively, even when the geometry configuration is poor.

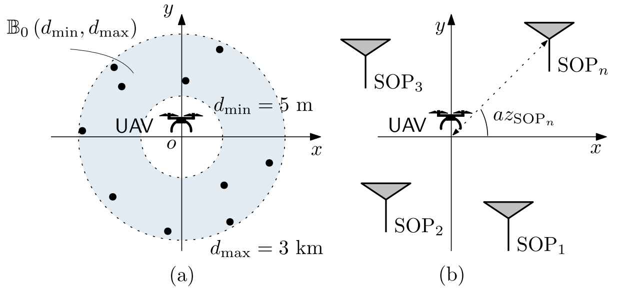

Fig. 9. (a) BPP realization with $N = 10$. (b) The azimuth angles in a BPP are uniformly distributed between 0 and 2π.

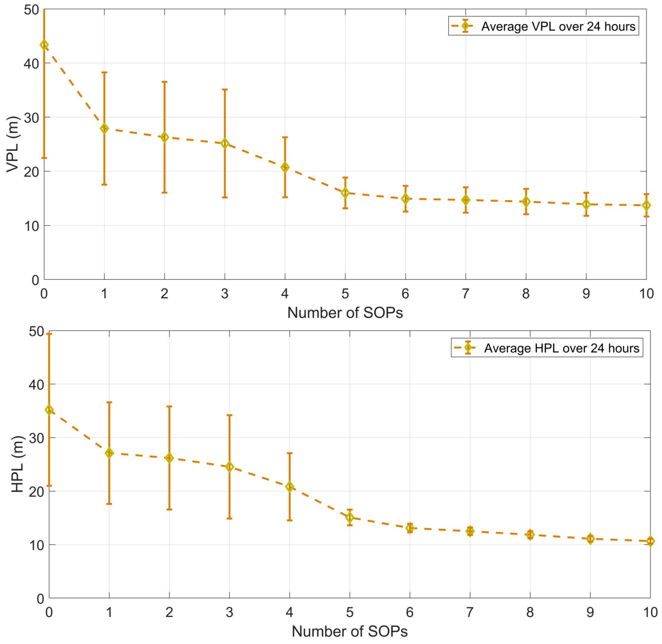

Fig. 10. Impact of the number of SOPs on the achieved PLs over a 24-hour period. The vertical lines in each plot represent the error bar.

D. Considering Other GNSS Constellations

The results presented in Subsection VI-A only considered GPS. In order to study the reduction in PL via adding SOP measurements, while considering other GNSS constellations the simulation setup presented in Subsection VI-A was extended to account for both GPS and GLONASS. To this end, the GLONASS satellites' Keplerian elements

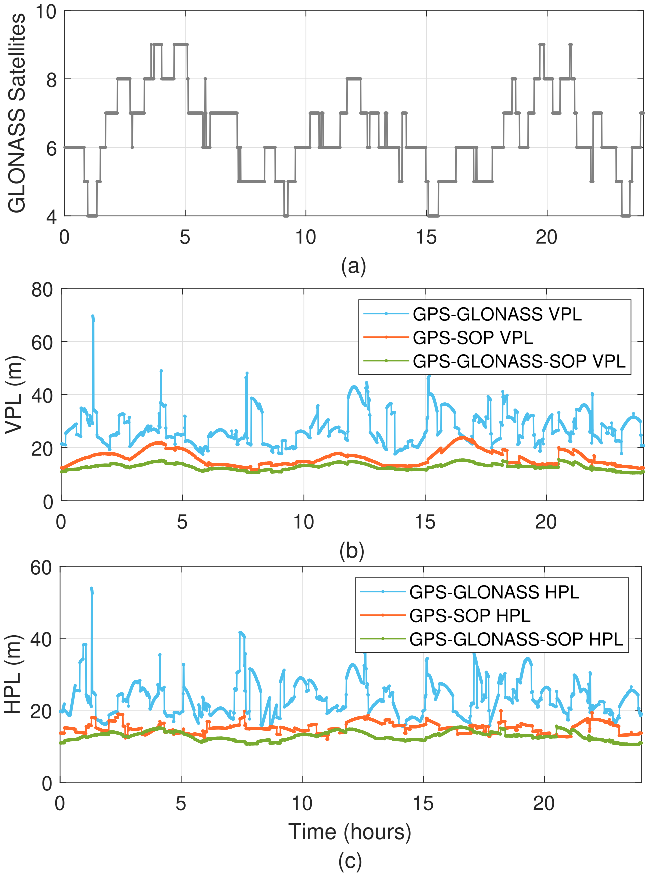

Fig. 11. Simulation results for a GNSS-based navigation system: (a) The number of available GLONASS satellites for a 24-hour period. (b) Comparison between GPS-GLONASS and GPS-GLONASS-SOP PLs over 24 hours. (c) Comparison between GPS-GLONASS and GPS-GLONASS-SOP HPLs over 24 hours.

parameterizing the orbits were extracted from the North American Aerospace Defense Command (NORAD) publicly available database [72]. The orbit's parameters are updated daily in the two-line element (TLE) files. Using TLEs and orbit determination algorithms, the positions and velocities of the GLONASS satellites were calculated for the time and location described in Subsection VI-A. Fig. 11 (a) illustrates the associated number of available GLONASS satellites for a 24-hour period. Fig. 11 (b)-(c) illustrate the VPL and HPL obtained by the GPS-GLONASS solution (blue line), GPS-SOP solution (orange line), and the proposed GPS-GLONASS-SOP solution (green line). Over 24-hours, the average GPS-GLONASS VPL was 27.28 m, the average GPS-SOP VPL was 15.59 m, and the average GPS-GLONASS-SOP VPL was 12.82 m. By comparing Fig. 7 and Fig. 11, it is evident that even in GNSS-based navigation systems, introducing SOP measurements can reduce the VPL by more than 50%. It is important to note that while the number of SOPs were fixed to 5, the number of GLONASS satellites was greater than or equal to 5 in about 99% of the time over 24-hours. Therefore, another important conclusion that can be drawn from this plot is that while the number of GLONASS satellites is more than the SOP transmitters, adding SOP transmitters is more effective in reducing the PLs (compare orange and blue lines). This shows the effectiveness of the proposed method, validating that while adding more measurements from other satellite constellations decreases the PL, measurements from transmitters at (i) low elevation angles are more effective in minimizing the VPL than transmitters at elevation angles between 0 and 90 degrees and (ii) uniformly distributed azimuth angles (which is inherent in certain SOPs by construction, e.g., cellular SOPs), are more effective in minimizing the HPL.

E. Evaluating SOP Clock Model Mismatch

In Section IV, the mismatch between the time evolution of the true clock bias and its first-order polynomial approximation was analyzed. This subsection analyzes the impact of this mismatch component on the measurement error. Define

$$\delta t_{\text{SOP}_n}(k) \triangleq \dot{\delta t}_{\text{SOP}_n} kT + \delta t_{\text{SOP}_{n,0}} + \eta_{r,s_n},$$

where η_{r,s_n} is the mismatch between the true time evolution of $\delta t_{\text{SOP}_n}(k)$ and its first-order approximation. In [43], it was shown that η_{r,s_n} is a zero-mean white random sequence with variance σ^2_{η,r,s_n} and is obtained from the k-th element of the vector

$$\boldsymbol{\eta}_{r,s_n} = \mathbf{G}\mathbf{F_1}\mathbf{w_1} + \mathbf{G}\mathbf{F_2}\mathbf{w_2}, \tag{2}$$

where

$$\mathbf{w_1} \triangleq \left[w_{\delta t_{r,s_n}}(0), \ldots, w_{\delta t_{r,s_n}}(K-2)\right]^{\mathsf{T}},$$

$$\mathbf{w_2} \triangleq \left[w_{\dot{\delta t}_{r,s_n}}(0), \ldots, w_{\dot{\delta t}_{r,s_n}}(K-3)\right]^{\mathsf{T}},$$

$$\mathbf{F_1} \triangleq \begin{bmatrix} 0 & 0 & \ldots & 0 \\ 1 & 0 & \ldots & 0 \\ \vdots & \vdots & \ddots & \vdots \\ 1 & 1 & \ldots & 1 \end{bmatrix}_{(K)\times(K-1)},$$

$$\mathbf{F_2} \triangleq \begin{bmatrix} 0 & 0 & \ldots & 0 \\ 0 & 0 & \ldots & 0 \\ T & 0 & \ldots & 0 \\ 2T & T & \ldots & 0 \\ \vdots & \vdots & \ddots & \vdots \\ (K-2)T & (K-3)T & \ldots & T \end{bmatrix}_{(K)\times(K-2)},$$

$$\mathbf{G} = \left[\mathbf{I} - \mathbf{S}(\mathbf{S}^{\mathsf{T}}\mathbf{S})^{-1}\mathbf{S}^{\mathsf{T}}\right], \quad \mathbf{S} \triangleq \begin{bmatrix} 0 & T & \ldots & (K-1)T \\ 1 & 1 & \ldots & 1 \end{bmatrix}^{\mathsf{T}},$$

where K is the total number of processed samples; $\mathbf{I}$ is the Identity matrix; and $w_{\delta t_{r,s_n}}$ and $w_{\dot{\delta t}_{r,s_n}}$ are the noise corresponding to the time evolution of the clock bias and clock drift, respectively. Equation (2) implies that the impact of the mismatch error component on the measurement accuracy depends on the quality of the oscillators used in the receiver and in the SOPs' transmitters. Fig. 12 shows σ_{η,r,s_n} for a transmitter equipped with a high-quality oven-controlled crystal oscillator (OCXO), which is a reasonable assumption [54], [73], and four different receivers: (i) a receiver equipped with a high-quality OCXO, (ii) a receiver equipped with a typical OCXO, a receiver equipped with a typical temperature-compensated crystal oscillator (TCXO), and (iv) a receiver equipped with a low-quality TCXO. From Fig. 12, one can see the conservativeness of the mismatch $\eta_{r,s_n}(k)$ due

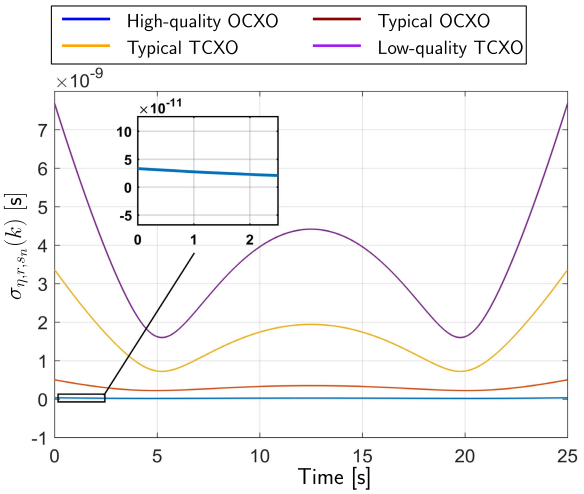

Fig. 12. The standard deviation $\{\sigma_{\eta,r,s_n}(k)\}_{k=0}^{K-1}$ of the vector $\boldsymbol{\eta}_{r,s_n}$ for four receivers, equipped with different oscillators: (i) high-quality OCXO, (ii) typical OCXO, (iii) typical TCXO, and (iv) low-quality TCXO. Here, $K = 2,500$ samples and $T = 0.01$ s.

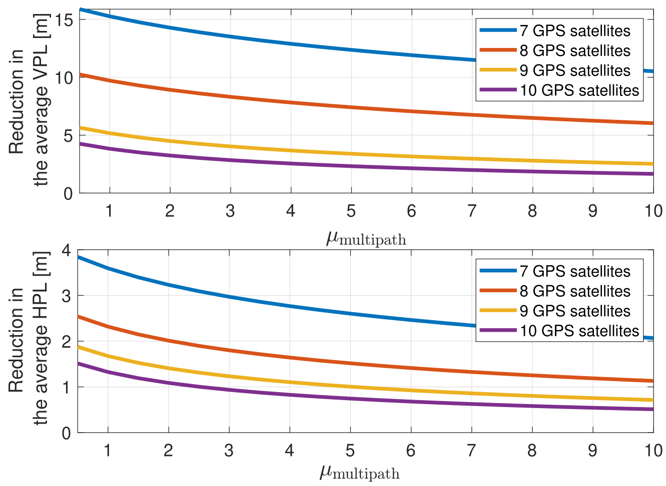

Fig. 13. The expected reduction in VPL and HPL by adding one SOP measurement into the navigation system in a multipath environment. These tests were performed at 10 degrees elevation mask.

to different clock types. The clock bias process noise power spectral densities of the receivers equipped with high-quality OCXO, typical OCXO, typical TCXO, and low-quality TCXO were set to be 1.3×10^{-22} s, 4×10^{-20} s, 4.7×10^{-20} s, and 1×10^{-19} s respectively. As it can be seen from Fig. 12, the mismatch error standard deviation component in the receiver equipped with a high-quality OCXO is about 1 centimeter and in the receiver equipped with a typical OCXO is nearly 10 centimeters. Comparing this with the cdf-overbound variances calculated in Section IV validates that using a first-order polynomial for a fairly stable oscillator is conservative.

F. Evaluating the Effect of Multipath on SOPs

Although cellular SOPs undergo severe multipath effects due to the low elevation angle of the received signal, the literature have shown that the high transmission bandwidth of these signals make them more robust to multipath compared to GNSS signals [74]. Cellular SOP multipath analysis for navigation in urban environment has been investigated in [23], [75], [76], where the statistics of the measurement error in a multipath and multipath-free environment was analyzed. It was shown that the multipath error can be reduced from 15 m to 50 cm by increasing bandwidth from 1.4 MHz to 20 MHz. The impact of the SOP multipath on the integrity of the navigation solution was discussed in [43]. In this subsection, the impact of SOP short multipath delay on VPL reduction is evaluated. For this analysis, LTE SOP is considered. This methodology can be applied to other terrestrial SOP types. In the case of short multipath delays, biases will be induced in the pseudorange measured by the receiver. In [77], a method was proposed to characterize this bias using the channel impulse response (CIR). It was shown that the induced bias can be formulated according to

$$b_n = c\frac{\chi_n}{\kappa}, \quad \kappa \triangleq -\frac{4\pi A^2 \cos\left(\frac{\pi}{2M}\right)}{M\left[\sin\left(\frac{\pi}{2M}\right)\right]^3}, \tag{3}$$

where $M \triangleq \left\lfloor \frac{N_r}{6} \right\rfloor$, N_r denotes the number of subcarriers in the received LTE signal, A denotes signal amplitude, and $\lfloor . \rfloor$ denotes the integer floor function. The term χ_n in (3) denotes the effect of multipath interference on the receiver's delay-locked loop (DLL) and is function of the subcarrier interval, the DLL correlator spacing, the number of subcarrier symbols in the LTE pilot signal, the signal power due to antenna gain and implementation loss, and the normalized symbol timing error. As one can expect, in the presense of significant multipath, this error component gets larger values, therefore, its contribution to the measurement noise gets larger. This effect can be characterized by increasing the ratio between the SOP measurement noise (which has been corrupted by multipath) and GPS measurement noise. In fact, inflating the measurement noise variance to account for multipath is a well-known technique in the multipath mitigation approaches that has been proposed in the literature [78], [79]. Accordingly, it is proposed that the induced bias can be characterized by adding an inflation term to the SOP measurement error. This inflation factor can be formulated as $\mu_{\text{multipath}} \triangleq \sigma^2_{\text{SOP}}/\sigma^2_{\text{GPS}}$. To evaluate the effect of incorporating SOPs in multipath environment, the analysis presented in Section V was performed by swiping the inflation factor $\mu_{\text{multipath}}$ from 0.5 to 10. The results are shown in Fig. 13, where the expected reduction by incorporating one SOP is plotted, considering different values for $\mu_{\text{multipath}}$ and different number of pre-existing GPS satellites. From this figure, it can be seen that the VPL and HPL reduction does not change significantly by increasing $\mu_{\text{multipath}}$, especially for the cases where 8 or more satellites are available in the environment. It is important to mention that this analysis does not aim at formulating SOP multipath, which has been already formulated in (3). In contrast, this analysis aim at evaluating the impact of SOP multipath on the expected reduction in the VPL via the proposed method. Therefore, from Fig. 13, it can be concluded that even in the multipath environments, introducing the SOP transmitter will reduce the PLs. It is evident from this figure that when

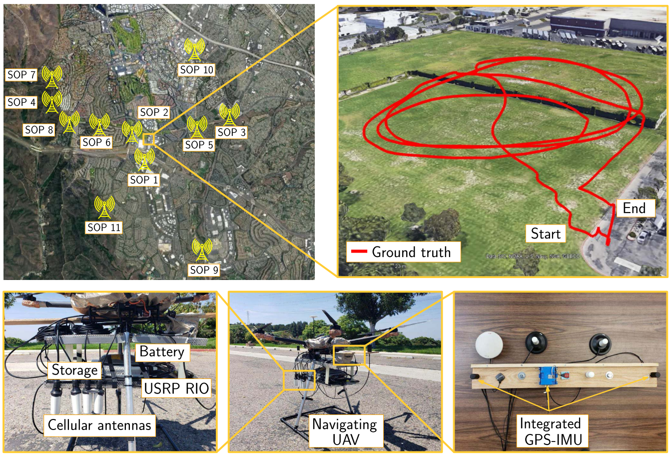

Fig. 14. Experimental hardware setup and the traversed trajectory along with the position of cellular LTE SOP towers.

multipath is high, this reduction is less. However, even in multipath environments, incorporating SOP transmitters will not negatively contribute in VPL calculations.

VII. Experimental Results

This section describes the experimental hardware setup and presents the results demonstrating the proposed GNSS-SOP framework for UAV PL reduction.

A. Hardware Setup

A DJI Matrice 600 drone was equipped with a National Instrument (NI) universal software radio peripheral (USRP)-2955 to sample LTE signals at four different carrier frequencies. For this experiment, LTE carrier frequencies 1955, 2145, 2125, and 739 MHz were used, which are allocated to USA operators AT&T, T-Mobile, and Verizon. The sampling rate was set to 10 MSps and the sampled LTE signals were recorded on a laptop. The UAV was also equipped with a Septentrio AsteRx-i V integrated GNSS-IMU sensor [80]. Over the course of the experiment, the ground-truth trajectory of the UAV was obtained from this integrated GNSS-IMU navigation system, while the raw GPS measurements were used to estimate the receiver's position via the framework presented in Section III and to calculate the PL via the approach presented in Section V. Septentrio's post-processing software development kit (PP-SDK) was used to process carrier phase observables collected by the AsteRx-i V and by a nearby differential GPS base station to obtain a carrier phase-based navigation solution. This integrated GNSS-IMU real-time kinematic (RTK) system was used to produce the ground-truth results with which the proposed navigation framework was compared. Fig. 14 shows the experimental hardware setup, the environmental layout of the experiment, the location of the SOP towers, and the ground truth.

Over the course of the experiment, the receiver traversed a trajectory of 823 m over 240 s, while listening to 11 cellular LTE SOP towers. The locations of the towers in the environment were mapped before the experiment. The towers' cell IDs and their corresponding carrier frequencies are presented in Table V.

TABLE V
SOP Towers' Characteristics

Cell ID	Carrier frequency (MHz)
78	2145
104, 352	1955
308, 358, 224, 58, 354	2125
492, 5, 27	739

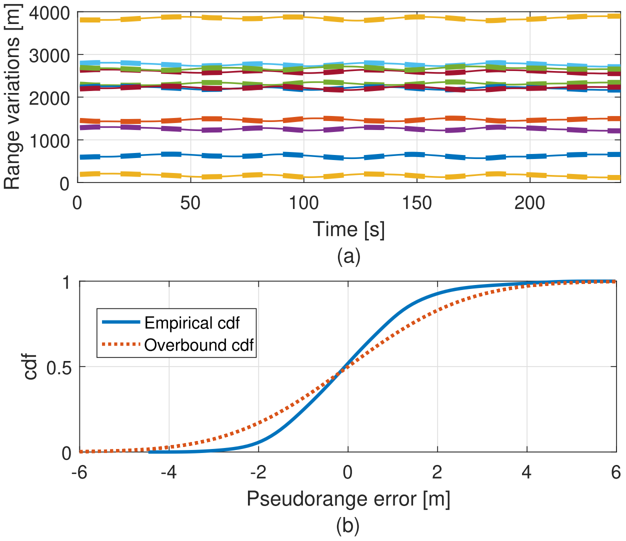

Fig. 15. (a) LTE pseudorange (solid lines) and true range (dashed lines) variations for towers 1 through 11 (different colors correspond to different towers). (b) Empirical cdf and the overbound cdf of the LTE pseudoranges for towers 1 through 11.

The sampled LTE signals were processed offline using the proposed LTE SDR in [23], which was developed in MATLAB. The resulting measurements were used to estimate the receiver's location using the proposed navigation framework.

B. Experimental Results

1) Measurements: Fig. 15 (a) shows LTE pseudorange (solid lines) and true range (dashed lines) variations and Fig. 15 (b) shows the empirical cdf of the LTE pseudorange measurement errors. The overbound cdf obtained from the DeCleene' method [63] are overlayed on this plot. The pseudorange measurement errors were obtained by subtracting the pseudorange measurement from the true range measurement, i.e., $z_{\text{SOP}_n}(k) - \left\| \boldsymbol{r}_r(k) - \boldsymbol{r}_{\text{SOP}_n}(k) \right\|_2$, for $n = 1, \ldots, 11$. The true ranges are known from the knowledge of the transmitters' location and receiver's ground truth position, which was obtained from the integrated GNSS-IMU RTK system. The standard deviations of the pseudoranges for towers 1 through 11 were calculated to be 0.95, 1.54, 0.8, 1.72, 1.03, 1.74, 1.30, 1.78, 1.43, 0.86, and 1.28 m, respectively. It is worth noting that one cannot fairly compare the results of these

TABLE VI

COMPARISON BETWEEN NAVIGATION SOLUTION PERFORMANCE

Scenario	**2-D RMSE [m]**	**3-D RMSE [m]**	**Average HPE [m]**	**Average HPL [m]**	**Average VPE [m]**	**Average VPL [m]**
GPS-only solution	2.34	4.37	2.34	26.32	3.70	27.83
GPS-SOP solution	1.13	3.63	1.13	4.64	3.44	11.99
Reduction	51.46%	16.98%	51.7%	82.37%	7.02%	56.91%

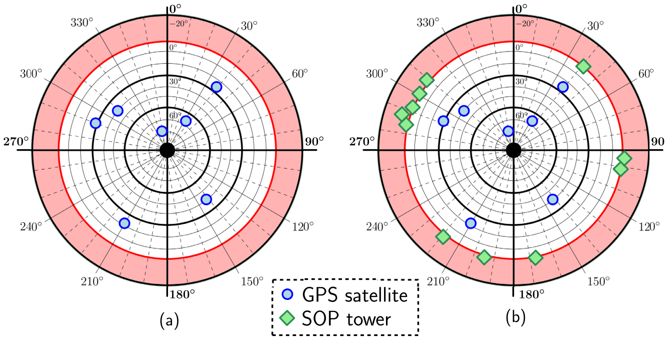

Fig. 16. Sky plot of GPS satellites and SOP towers over Aliso Viejo, California, USA at 4:40 pm, coordinated universal time (UTC), June 16, 2019. The sky plot shows elevation and azimuth angles of transmitters. The red region corresponds to the negative elevation angles, at which the SOPs' measurements were received. (a) GPS satellites. (b) GPS satellites and SOP towers.

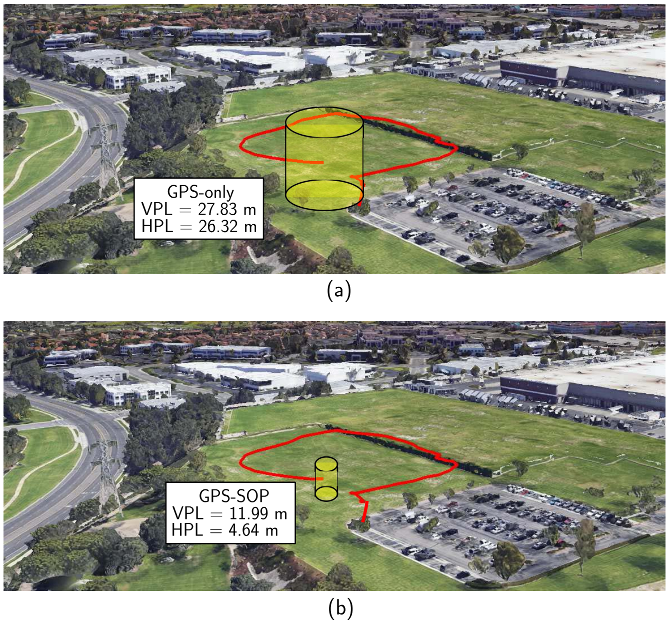

Fig. 17. Comparison between GPS-only and GPS-SOP frameworks. It is evident that incorporating the SOP signals significantly reduces the PLs.

measurements with each other since the received signals from these towers have experienced different carrier-to-noise ratio and multipath conditions.

2) Adding SOPs in the GPS-Based Navigation System: The UAV flew for 240 s, while collecting LTE signals from 11 LTE towers in the environment. The stored LTE signals were then processed by the LTE module of the MATRIX SDR to produce LTE SOP pseudoranges, which were then fused with raw GPS pseudorange measurements obtained from the Septentrio receiver to produce the navigation solution along with the corresponding VPL and HPL. Two sets of results were produced to evaluate the impact of SOP measurements on navigation and on PL: (i) a navigation solution and MHSS RAIM-based PL measures using GPS measurements only and (ii) a navigation solution and MHSS RAIM-based PL using GPS and cellular SOP measurements. The 2-D and 3-D position root-mean squared errors (RMSEs) and the vertical position error (VPE) are tabulated in Table VI for both navigation solutions: GPS-only and GPS-SOP. As it can been from Table VI, incorporating the proposed method reduced the VPL and HPL by 56.91% and 82.37%, respectively. However, comparing the VPLs of GPS-only and GPS-SOP systems alone could be an incomplete comparison as these systems operate on different measurement sets. To address this concern, the gaps between VPL and VPE (i.e., VPL-VPE) is also considered. According to Table VI, the gap between VPL and VPE in GPS-only system is 24.13 m, while the gap between VPL and VPE in GPS-SOP system is 8.55 m. This indicates that the proposed approach was able to provide the navigation system with a tighter vertical bound. As can be seen from Table VI, incorporating SOPs resulted more reduction in the HPL, compared to the VPL. This happened based on the geometric distribution of the satellites in this experiment. The change in the satellites' geometric configuration will result in different reduction rates in HPL and VPL.

Fig. 16 (a) illustrates the GPS satellites' sky plot over Aliso Viejo, California, USA at time 4:40 pm, coordinated universal time (UTC), on June 16, 2019. The elevation and azimuth angles of GPS satellites were computed using GPS ephemeris files extracted from the recorded RINEX file. Fig. 16 (b) illustrates the sky plot for both GPS and SOP transmitters. The red region in Fig. 16 (a)–(b) corresponds to negative elevation angles, at which the SOPs' measurements were received. For a comparative analysis, the results achieved by the proposed framework is compared to the results achieved by the GBAS framework presented in [53], where it was shown that the VPL and HPL are reduced by 57% and 65%, respectively, when GBAS corrections were used. While the VPL reduction obtained from GBAS is comparable with that obtained from SOPs, the HPL reduction obtained with SOPs is larger than GBAS. Moreover, SOP towers are more abundant than GBAS infrastructure, and SOPs are not limited to airport vicinities; hence, and UAVs navigating in urban environments could benefit from SOPs' transmitted signals.

Fig. 17 (a)–(b) shows the calculated PLs without and with incorporating the SOP signals, respectively.

3) Adding SOPs in the GNSS-Based Navigation System: Next, the impact of adding SOPs in the GNSS-based navigation framework was evaluated. To this end, the experimental results were extended to account for both GPS and GLONASS

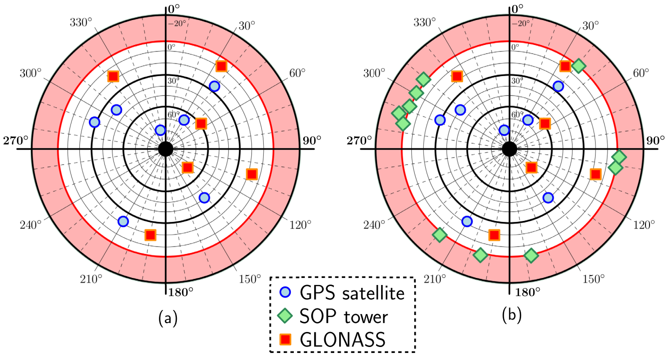

Fig. 18. Sky plot of GNSS satellites and SOP towers over Aliso Viejo, California, USA. (a) GNSS satellites. (b) GNSS satellites and SOP towers.

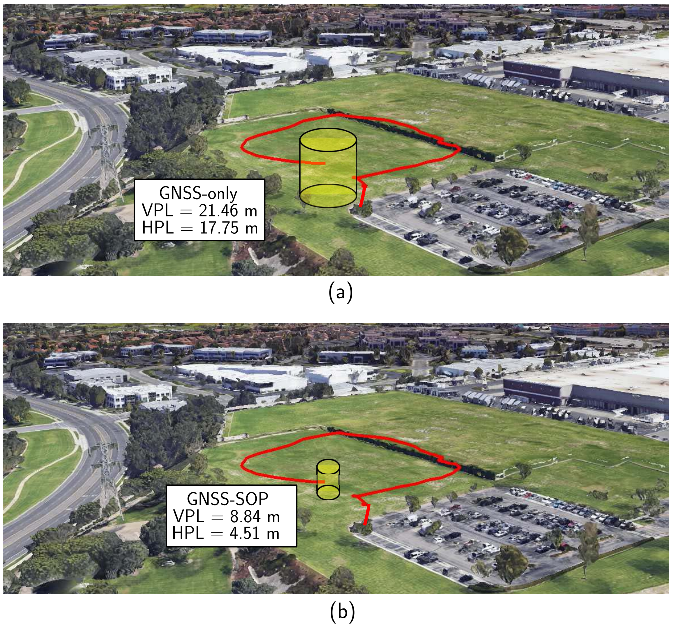

Fig. 19. Comparison between the PLs of (a) GNSS-only and (b) GNSS-SOP frameworks.

satellites. The GLONASS satellites' Keplerian elements parameterizing the orbits were extracted from the navigation RINEX file produced by the Septentrio receiver. Similarly, the GLONASS pseudorange measurements were extracted from the observation RINEX file. Fig. 18 (a) illustrates the GPS and GLONASS satellites' sky plot, while Fig. 18 (b) illustrates the sky plot for the GPS, GLONASS, and SOP transmitters. Fig. 19 (a) and Fig. 19 (b) shows the calculated VPL and HPL using GNSS measurements and using GNSS plus SOP measurements, respectively.

The VPL of the GNSS-only navigation solution was 21.46 m, while the VPL of the proposed GNSS-SOP was 8.84 m. The HPL of the GNSS-only navigation solution was 17.75 m, while the HPL of the proposed GNSS-SOP was 4.51 m. Hence, incorporating the developed framework in this paper reduced the VPL and HPL by 58.8% and 74.6%, respectively. Note that the GNSS-SOP HPL is larger than the GPS-SOP HPL. This could be due to the increased dimensionality of the RAIM algorithm by adding more measurements. More importantly, adding SOPs to GPS only and GNSS improves their respective performances.

VIII. CONCLUSION

This paper developed a method for reducing the VPL and HPL for a UAV by incorporating SOP measurements into both GPS-based and GNSS-based navigation systems. First, the statistics of cellular SOP measurement errors were characterized from extensive data collected over the past few years in different environments and from different providers, transmitting at different frequencies and bandwidths. Then, It was demonstrated that the VPL of the GNSS-only solution can be reduced by exploiting the inherently small elevation angles of terrestrial SOPs and the HPL can be reduced by exploiting the SOPs' well-spaced azimuth angles. The impact of common SOP measurement errors were evaluated, including clock bias and multipath errors. Finally, a real-world experimental test over a total traversed trajectory of 823 m was performed to validate the efficacy of the proposed framework. Results showed that introducing the SOP measurements into GPS and GNSS navigation systems reduced VPL by 56.9% and 58.8%, respectively, while the HPL was reduced by 82.4% and 74.6%, respectively. It is important to note that the GNSS satellite configuration benefits from more favorable geometry, compared to GPS-only satellite configuration. As a result, it is harder to improve the GNSS-geometry further by incorporating SOPs, compared to improving the GPS-only geometry. Nevertheless, as shown in the paper, incorporating SOPs reduces the HPL and VPL for both GPS-only and GNSS-only. Although it was shown that incorporating SOPs can improve both navigation accuracy and reduce the PL, the lack of commitment from SOP providers can be considered as a drawback of the proposed approach, which could be the subject of future work.

ACKNOWLEDGMENT

The authors would like to thank Kimia Shamaei for her help with data collection and processing.

REFERENCES

[1] T. Murfin, "UAV report: Growth trends & opportunities for 2019," *GPS World Mag.*, vol. 29, no. 10, pp. S2–S9, Oct. 2018.

[2] Z. M. Kassas, P. Closas, and J. Gross, "Navigation systems panel report navigation systems for autonomous and semi-autonomous vehicles: Current trends and future challenges," *IEEE Aerosp. Electron. Syst. Mag.*, vol. 34, no. 5, pp. 82–84, May 2019.

[3] S. M. Saab and Z. M. Kassas, "Power matching approach for GPS coverage extension," *IEEE Trans. Intell. Transp. Syst.*, vol. 7, no. 2, pp. 156–166, Jun. 2006.

[4] J.-I. Meguro, T. Murata, J.-I. Takiguchi, Y. Amano, and T. Hashizume, "GPS multipath mitigation for urban area using omnidirectional infrared camera," *IEEE Trans. Intell. Transp. Syst.*, vol. 10, no. 1, pp. 22–30, Mar. 2009.

[5] C. Rose, J. Britt, J. Allen, and D. Bevly, "An integrated vehicle navigation system utilizing lane-detection and lateral position estimation systems in difficult environments for GPS," *IEEE Trans. Intell. Transp. Syst.*, vol. 15, no. 6, pp. 2615–2629, Dec. 2014.

[6] R. T. Ioannides, T. Pany, and G. Gibbons, "Known vulnerabilities of global navigation satellite systems, status, and potential mitigation techniques," *Proc. IEEE*, vol. 104, no. 6, pp. 1174–1194, Jun. 2016.

[7] D. Borio, F. Dovis, H. Kuusniemi, and L. L. Presti, "Impact and detection of GNSS jammers on consumer grade satellite navigation receivers," *Proc. IEEE*, vol. 104, no. 6, pp. 1233–1245, Jun. 2016.

[8] R. Toledo-Moreo, D. Betaille, and F. Peyret, "Lane-level integrity provision for navigation and map matching with GNSS, dead reckoning, and enhanced maps," *IEEE Trans. Intell. Transp. Syst.*, vol. 11, no. 1, pp. 100–112, Mar. 2010.

[9] D. Salos, "Integrity monitoring applied to the reception of GNSS signals in urban environments," Ph.D. dissertation, Dept. Mathématiques Informatique Télécommun., Nat. Polytech. Inst. Toulouse, Univ. Toulouse, Toulouse, France, 2012.

[10] K. Ansari, Y. Feng, and M. Tang, "A runtime integrity monitoring framework for real-time relative positioning systems based on GPS and DSRC," *IEEE Trans. Intell. Transp. Syst.*, vol. 16, no. 2, pp. 980–992, Apr. 2015.

[11] N. Zhu, J. Marais, D. Betaille, and M. Berbineau, "GNSS position integrity in urban environments: A review of literature," *IEEE Trans. Intell. Transp. Syst.*, vol. 19, no. 9, pp. 2762–2778, Sep. 2018.

[12] Q. Sun and J. Zhang, "RAIM method for improvement on GNSS reliability and integrity," in *Proc. IEEE/AIAA 28th Digit. Avionics Syst. Conf.*, Oct. 2009, pp. 3–11.

[13] J. Rife, S. Pullen, P. Enge, and B. Pervan, "Paired overbounding for nonideal LAAS and WAAS error distributions," *IEEE Trans. Aerosp. Electron. Syst.*, vol. 42, no. 4, pp. 1386–1395, Oct. 2006.

[14] A. Ene, J. Blanch, and T. Walter, "Galileo-GPS RAIM for vertical guidance," in *Proc. Nat. Tech. Meeting Inst. Navigat.*, Jan. 2006, pp. 18–20.

[15] T. Walter, J. Blanch, M. J. Choi, T. Reid, and P. Enge, "Incorporating GLONASS into aviation RAIM receivers," in *Proc. Int. Tech. Meeting Inst. Navigat.*, Jan. 2013, pp. 239–249.

[16] P. Roysdon and J. Farrell, "GPS-INS outlier detection and elimination using a sliding window filter," in *Proc. Amer. Control Conf.*, May 2017, pp. 1244–1249.

[17] A. V. Kanhere and G. X. Gao, "Integrity for GPS/LiDAR fusion utilizing a RAIM framework," in *Proc. 31st Int. Tech. Meeting Satell. Division Inst. Navigat. (ION GNSS+)*, Oct. 2018, pp. 3145–3155.

[18] J. McEllroy, "Navigation using signals of opportunity in the AM transmission band," M.S. thesis, Dept. Air Force, Air Force Inst. Technol., Air Univ., Wright-Patterson Air Force Base, OH, USA, 2006.

[19] A. Popleteev, "Indoor positioning using FM radio signals," Ph.D. dissertation, Univ. Trento, Trento, Italy, 2011.

[20] C. Yang and T. Nguyen, "Tracking and relative positioning with mixed signals of opportunity," *Navigation*, vol. 62, no. 4, pp. 291–311, Dec. 2015.

[21] J. Khalife and Z. M. Kassas, "Navigation with cellular CDMA signals—Part II: Performance analysis and experimental results," *IEEE Trans. Signal Process.*, vol. 66, no. 8, pp. 2204–2218, Apr. 2018.

[22] J. del Peral-Rosado, J. López-Salcedo, F. Zanier, and G. Seco-Granados, "Position accuracy of joint time-delay and channel estimators in LTE networks," *IEEE Access*, vol. 6, pp. 25185–25199, 2018.

[23] K. Shamaei and Z. M. Kassas, "LTE receiver design and multipath analysis for navigation in urban environments," *Navigation*, vol. 65, no. 4, pp. 655–675, Dec. 2018.

[24] Z. Kassas, A. Abdallah, and M. Orabi, "Carpe signum: Seize the signal—Opportunistic navigation with 5G," *Inside GNSS Mag.*, vol. 16, no. 1, pp. 52–57, 2021.

[25] L. Chen, O. Julien, P. Thevenon, D. Serant, A. G. Pena, and H. Kuusniemi, "TOA estimation for positioning with DVB-T signals in outdoor static tests," *IEEE Trans. Broadcast.*, vol. 61, no. 4, pp. 625–638, Dec. 2015.

[26] C. Yang, T. Nguyen, and E. Blasch, "Mobile positioning via fusion of mixed signals of opportunity," *IEEE Aerosp. Electron. Syst. Mag.*, vol. 29, no. 4, pp. 34–46, Apr. 2014.

[27] D. Lawrence *et al.*, "Navigation from LEO: Current capability and future promise," *GPS World Mag.*, vol. 28, no. 7, pp. 42–48, Jul. 2017.

[28] T. G. R. Reid, A. M. Neish, T. Walter, and P. K. Enge, "Broadband LEO constellations for navigation," *Navigation*, vol. 65, no. 2, pp. 205–220, Jun. 2018.

[29] Z. Kassas, J. Morales, and J. Khalife, "New-age satellite-based navigation—STAN: Simultaneous tracking and navigation with LEO satellite signals," *Inside GNSS Mag.*, vol. 14, no. 4, pp. 56–65, 2019.

[30] Z. Kassas, J. Khalife, M. Neinavaie, and T. Mortlock, "Opportunity comes knocking: Overcoming GPS vulnerabilities with other satellites' signals," *Inside Unmanned Syst. Mag.*, pp. 30–35, Jun./Jul. 2020.

[31] R. M. Faragher and R. K. Harle, "Towards an efficient, intelligent, opportunistic smartphone indoor positioning system," *Navigation*, vol. 62, no. 1, pp. 55–72, Mar. 2015.

[32] Y. Zhuang, Z. Syed, Y. Li, and N. El-Sheimy, "Evaluation of two WiFi positioning systems based on autonomous crowdsourcing of handheld devices for indoor navigation," *IEEE Trans. Mobile Comput.*, vol. 15, no. 8, pp. 1982–1995, Aug. 2016.

[33] R. Faragher, "Effects of multipath interference on radio positioning systems," Ph.D. dissertation, Dept. Phys., Univ. Cambridge, Cambridge, U.K., 2007.

[34] L. A. Merry, R. M. Faragher, and S. Schedin, "Comparison of opportunistic signals for localisation," in *Proc. IFAC Symp. Intell. Auton. Veh.*, Sep. 2010, pp. 109–114.

[35] J. Morales, J. Khalife, and Z. Kassas, "Opportunity for accuracy," *GPS World Mag.*, vol. 27, no. 3, pp. 22–29, Mar. 2016.

[36] M. Maaref and Z. M. Kassas, "UAV integrity monitoring measure improvement using terrestrial signals of opportunity," in *Proc. 32nd Int. Tech. Meeting Satell. Division Inst. Navigat. (ION GNSS+)*, Oct. 2019, pp. 3045–3056.

[37] E. Kaplan and C. Hegarty, *Understanding GPS: Principles and Applications*, 2nd ed. Norwood, MA, USA: Artech House, 2005.

[38] T. G. Needham and M. S. Braasch, "Gravity model error considerations for high-integrity GNSS-aided INS operations," in *Proc. IEEE/ION Position, Location Navigat. Symp. (PLANS)*, Apr. 2018, pp. 822–832.

[39] A. Hassani, N. Morris, M. Spenko, and M. Joerger, "Experimental integrity evaluation of tightly-integrated IMU/LiDAR including return-light intensity data," in *Proc. 32nd Int. Tech. Meeting Satell. Division Inst. Navigat. (ION GNSS+)*, Oct. 2019, pp. 2637–2658.

[40] J. E. Angus, "RAIM with multiple faults," *Navigation*, vol. 53, no. 4, pp. 249–257, Dec. 2006.

[41] M. Joerger, F. Chan, and B. Pervan, "Solution separation versus residual-based RAIM," *J. Navigat.*, vol. 61, no. 61, pp. 237–330, Jun. 2014.

[42] D. Borio and C. Gioia, "Galileo: The added value for integrity in harsh environments," *Sensors*, vol. 16, no. 1, p. 111, Jan. 2016.

[43] M. Maaref and Z. M. Kassas, "Measurement characterization and autonomous outlier detection and exclusion for ground vehicle navigation with cellular signals," *IEEE Trans. Intell. Vehicles*, vol. 5, no. 4, pp. 670–683, Dec. 2020.

[44] R. Brown and P. McBurney, "Self-contained GPS integrity checks using maximum solution separation as the test statistic," in *Proc. Int. Tech. Meeting Satell. Division The Inst. Navigat.*, Sep. 1987, pp. 263–268.

[45] B. S. Pervan, S. P. Pullen, and J. R. Christie, "A multiple hypothesis approach to satellite navigation integrity," *Navigation*, vol. 45, no. 1, pp. 61–71, Mar. 1998.

[46] J. Blanch *et al.*, "A proposal for multi-constellation advanced RAIM for vertical guidance," in *Proc. Int. Tech. Meeting Satell. Division The Inst. Navigat.*, Sep. 2011, pp. 2665–2680.

[47] J. Blanch *et al.*, "Advanced RAIM user algorithm description: Integrity support message processing, fault detection, exclusion, and protection level calculation," in *Proc. ION GNSS Conf.*, Sep. 2012, pp. 2828–2849.

[48] B. Belabbas, P. Remi, and M. Meurer, "Performance assessment of GBAS CAT III using GPS and Galileo," in *Proc. ION GNSS Conf.*, Sep. 2008, pp. 2945–2952.

[49] T. Dautermann, C. Mayer, F. Antreich, A. Konovaltsev, B. Belabbas, and U. Kälberer, "Non-Gaussian error modeling for GBAS integrity assessment," *IEEE Trans. Aerosp. Electron. Syst.*, vol. 48, no. 1, pp. 693–706, Jan. 2012.

[50] Z. Wang, C. Macabiau, J. Zhang, and A. Escher, "Prediction and analysis of GBAS integrity monitoring availability at LinZhi airport," *GPS Solutions*, vol. 18, pp. 27–40, 2014.

[51] R. Sabatini, T. Moore, and C. Hill, "Avionics-based GNSS integrity augmentation synergies with SBAS and GBAS for safety-critical aviation applications," in *Proc. IEEE/AIAA Digit. Avionics Syst. Conf.*, Sep. 2016, pp. 1–10.

[52] M. Caamano, M. Felux, M. Circiu-Simona, and D. Gerbeth, "Multi-constellation GBAS: How to benefit from a second constellation," in *Proc. IEEE/ION Position, Location Navigat. Symp.*, Apr. 2016, pp. 833–841.

[53] Y. Zhu, Y. Liu, Z. Wang, and Q. Li, "Evaluation of GBAS flight trials based on BDS and GPS," *IET Radar, Sonar, Navigat.*, vol. 14, no. 2, pp. 233–241, Feb. 2020.

[54] Z. Kassas, V. Ghadiok, and T. Humphreys, "Adaptive estimation of signals of opportunity," in *Proc. ION GNSS Conf.*, Sep. 2014, pp. 1679–1689.

[55] J. J. Morales and Z. M. Kassas, "Optimal collaborative mapping of terrestrial transmitters: Receiver placement and performance characterization," *IEEE Trans. Aerosp. Electron. Syst.*, vol. 54, no. 2, pp. 992–1007, Apr. 2018.

[56] A. Rodriguez, C. Tiberius, R. Bree, and Z. Geradts, "Google timeline accuracy assessment and error prediction," *Forensic Sci. Res.*, vol. 3, no. 3, pp. 240–255, 2018.

[57] General Data Resources, Inc. (2020). *Antenna Database*. [Online]. Available: http://antennasearch.com

[58] J. Morales and Z. Kassas, "Tightly-coupled inertial navigation system with signals of opportunity aiding," *IEEE Trans. Aerosp. Electron. Syst.*, vol. 57, no. 3, pp. 1930–1948, Jun. 2021.

[59] Z. M. Kassas and T. E. Humphreys, "Observability analysis of collaborative opportunistic navigation with pseudorange measurements," *IEEE Trans. Intell. Transp. Syst.*, vol. 15, no. 1, pp. 260–273, Feb. 2014.

[60] K. Shamaei, J. Khalife, and Z. Kassas, "Performance characterization of positioning in LTE systems," in *Proc. ION GNSS Conf.*, Sep. 2016, pp. 2262–2270.

[61] F. Knutti, M. Sabathy, M. Driusso, H. Mathis, and C. Marshall, "Positioning using LTE signals," in *Proc. Navigat. Conf. Eur.*, Apr. 2015, pp. 1–8.

[62] Z. Kassas, J. Khalife, A. Abdallah, and C. Lee, "I am not afraid of the jammer: Navigating with signals of opportunity in GPS-denied environments," in *Proc. ION GNSS Conf.*, Sep. 2020, pp. 1566–1585.

[63] B. DeCleene, "Defining pseudorange integrity-overbounding," in *Proc. Int. Tech. Meeting Satell. Division Inst. Navigat.*, Sep. 2000, pp. 1916–1924.

[64] GPS Directorate. (Sep. 2008). *Global Positioning System Standard Positioning Service Performance Standard (GPS SPS PS)*. [Online]. Available: http://www.gps.gov/technical/ps/

[65] L. Heng, "Safe satellite navigation with multiple constellations: Global monitoring of GPS and GLONASS signal-in-space anomalies," Ph.D. dissertation, Dept. Elect. Eng., Stanford Univ., Stanford, CA, USA, 2012.

[66] M. Jia, J. Khalife, and Z. Kassas, "Evaluation of ground vehicle protection level reduction due to fusing GPS with faulty terrestrial signals of opportunity," in *Proc. ION Int. Tech. Meeting*, Jan. 2021, pp. 354–365.

[67] *Minimum Operational Performance Standards for Global Positioning System/Wide Area Augmentation System Airborne Equipment*, RTCA, Washington, DC, USA, Dec. 2001.

[68] V. Kropp and G. Berz, "Optimized MHSS ARAIM user algorithms: Assumptions, protection level calculation and availability analysis,"' in *Proc. IEEE/ION Position, Location Navigat. Symp. (PLANS)*, May 2014, pp. 308–323.

[69] M. Haenggi, J. G. Andrews, F. Baccelli, O. Dousse, and M. Franceschetti, "Stochastic geometry and random graphs for the analysis and design of wireless networks," *IEEE J. Sel. Areas Commun.*, vol. 27, no. 7, pp. 1029–1046, Sep. 2009.

[70] K. Shamaei and Z. Kassas, "Sub-meter accurate UAV navigation and cycle slip detection with LTE carrier phase," in *Proc. ION GNSS Conf.*, Sep. 2019, pp. 2469–2479.

[71] J. Khalife and Z. Kassas, "Opportunistic UAV navigation with carrier phase measurements from asynchronous cellular signals," *IEEE Trans. Aerosp. Electron. Syst.*, vol. 56, no. 4, pp. 3285–3301, Aug. 2020.

[72] North American Aerospace Defense Command (NORAD). *Two-Line Element Sets*. Accessed: Feb. 23, 2020. [Online]. Available: http://celestrak.com/NORAD/elements/

[73] K. Wesson, K. Pesyna, J. Bhatti, and T. Humphreys, "Opportunistic frequency stability transfer for extending the coherence time of GNSS receiver clocks," in *Proc. ION GNSS Conf.*, Sep. 2010, pp. 2959–2968.

[74] S. Aditya, A. F. Molisch, and H. M. Behairy, "A survey on the impact of multipath on wideband time-of-arrival based localization," *Proc. IEEE*, vol. 106, no. 7, pp. 1183–1203, Jul. 2018.

[75] C. Gentner, T. Jost, W. Wang, S. Zhang, A. Dammann, and U.-C. Fiebig, "Multipath assisted positioning with simultaneous localization and mapping," *IEEE Trans. Wireless Commun.*, vol. 15, no. 9, pp. 6104–6117, Sep. 2016.

[76] C. Yang and A. Soloviev, "Positioning with mixed signals of opportunity subject to multipath and clock errors in urban mobile fading environments," in *Proc. 31st Int. Tech. Meeting Satell. Division Inst. Navigat. (ION GNSS+)*, Oct. 2018, pp. 223–243.

[77] B. Yang, K. B. Letaief, R. S. Cheng, and Z. Cao, "Timing recovery for OFDM transmission," *IEEE J. Sel. Areas Commun.*, vol. 18, no. 11, pp. 2278–2291, Nov. 2000.

[78] F. Nievinski, "Forward and inverse modeling of GPS multipath for snow monitoring," Ph.D. dissertation, Univ. Colorado, Boulder, CO, USA, 2013.

[79] S. Tay and J. Marais, "Weighting models for GPS pseudorange observations for land transportation in urban canyons," in *Proc. Eur. Workshop GNSS Signals Signal Process.*, Dec. 2013, pp. 1–4.

[80] (2018). *Septentrio AsteRx-i V*. [Online]. Available: https://www.septentrio.com/products

Mahdi Maaref received the B.S. and M.S. degrees from the University of Tehran in 2008 and 2011, respectively, and the Ph.D. degree in electrical engineering from Shahid Beheshti University in 2016. In 2016, he was a Visiting Research Collaborator with the University of Alberta, Edmonton, Canada. He is currently a Post-Doctoral Research Fellow with the University of California, Irvine. He is a member of the Autonomous Systems Perception, Intelligent, and Navigation (ASPIN) Laboratory. His research interests include autonomous ground vehicles, opportunistic perception, and autonomous integrity monitoring.

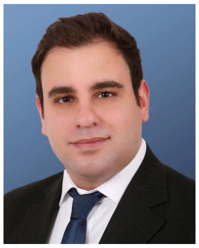

Joe Khalife (Member, IEEE) received the B.E. degree in electrical engineering and the M.S. degree in computer engineering from Lebanese American University (LAU), and the Ph.D. degree in electrical engineering and computer science from the University of California, Irvine. From 2012 to 2015, he was a Research Assistant at LAU. Since 2015, he has been a member of the ASPIN Laboratory. He is currently a Post-Doctoral Fellow with the University of California, Irvine. He is a member of the Autonomous Systems Perception, Intelligence, and Navigation (ASPIN) Laboratory. His research interests include opportunistic navigation, autonomous vehicles, and software-defined radio. He was a recipient of the 2016 IEEE/ION Position, Location, and Navigation Symposium (PLANS) Best Student Paper Award and the 2018 IEEE Walter Fried Award.

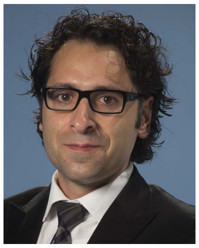

Zaher (Zak) M. Kassas (Senior Member, IEEE) received the B.E. degree in electrical engineering from Lebanese American University, the M.S. degree in electrical and computer engineering from The Ohio State University, and the M.S.E. degree in aerospace engineering and the Ph.D. degree in electrical and computer engineering from The University of Texas at Austin. He is currently an Associate Professor with the University of California, Irvine, and the Director of the Autonomous Systems Perception, Intelligence, and Navigation (ASPIN) Laboratory. He is also the Director of the U.S. Department of Transportation, Center for Automated Vehicles Research with Multimodal AssurEd Navigation (CARMEN), focusing on navigation resiliency and security of highly automated transportation systems. His research interests include cyber-physical systems, estimation theory, navigation systems, autonomous vehicles, and intelligent transportation systems. He was a recipient of the 2018 National Science Foundation (NSF) Faculty Early Career Development Program (CAREER) Award, the 2019 Office of Naval Research (ONR) Young Investigator Program (YIP) Award, the 2018 IEEE Walter Fried Award, the 2018 Institute of Navigation (ION) Samuel Burka Award, and the 2019 ION Col. Thomas Thurlow Award. He is an Associate Editor for the IEEE TRANSACTIONS ON AEROSPACE AND ELECTRONIC SYSTEMS and the IEEE TRANSACTIONS ON INTELLIGENT TRANSPORTATION SYSTEMS.